


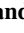


Statistical Analysis of Off-Great Circle Radio Wave Propagation in the Polar Cap

T. G. Cameron¹ , R. A. D. Fiori¹ , G. W. Perry² , A. Spicher³ , and T. Thayaparan⁴

¹Canadian Hazards Information Service, Natural Resources Canada, Ottawa, ON, Canada, ²Center for Solar-Terrestrial Research, New Jersey Institute of Technology, Newark, NJ, USA, ³Department of Physics and Technology, UIT the Arctic University of Norway, Tromsø, Norway, ⁴Defence Research and Development Canada, Ottawa Research Centre, Ottawa, ON, Canada

Key Points:

- Off-great circle propagation occurring in the polar cap is studied using years of data from an HF radio link in the polar cap
- Large (greater than 30°) deflections from the great circle are shown to be very common, especially in the winter
- These deflections are shown to affect HF radio signals in ways that are consistent with interactions with polar cap patches and arcs

Correspondence to:

T. G. Cameron,
taylor.cameron@NRCan-RNCan.gc.ca

Citation:

Cameron, T. G., Fiori, R. A. D., Perry, G. W., Spicher, A., & Thayaparan, T. (2024). Statistical analysis of off-great circle radio wave propagation in the polar cap. *Radio Science*, 59, e2023RS007897. <https://doi.org/10.1029/2023RS007897>

Received 30 OCT 2023

Accepted 22 MAR 2024

Abstract High latitude ionospheric density structures such as polar cap patches and arcs are capable of deflecting high frequency (HF) radio waves to off-great circle paths, and are likely detrimental to technologies dependent on HF radio propagation. In this study, nearly 2.5 years of 4.6–14.4 MHz data from a multi-frequency HF radio link between Qaanaaq, Greenland and Alert, Canada are used to investigate high-latitude off-great circle propagation in the polar cap. After an example of HF radio propagation affected by polar cap patches is shown in detail, a statistical analysis of the occurrence and impacts of off-great circle deflections in the polar cap is presented. Off-great circle propagation is shown to be increasingly common with increasing frequency up to 11.1 MHz, such that averaged over 1 year, received 11.1 MHz signals experienced deflections >30° from the great circle direction 65.6% of the time. The occurrence of these deflections across the year is shown to be at a maximum in the winter, while occurrence across the day varies with season. Trends across both time of day and time of year for 11.1 and 14.4 MHz deflections are consistent with polar cap patch occurrence trends. Off-great circle deflections are shown to be associated with increased time-of-flights, a larger range of positive and negative Doppler shifts, increased Doppler spreads, and lower signal-to-noise ratios. These results are discussed in the context of ionospheric phenomena in the polar cap, and implications for over-the-horizon radars operating at high latitudes.

Plain Language Summary High frequency (HF) radio waves can travel long distances by bouncing between the ground and the ionosphere; an upper layer of the Earth's atmosphere, allowing them to be used for communications and surveillance in remote locations. However, strong space weather can change the paths these radio waves take, causing problems for HF radio technologies. In this paper, radio transmissions sent between Qaanaaq, Greenland and Alert, Canada are studied in order to better understand how often HF radio waves are deflected by space weather at high latitudes, and what effect these deflections have on the signals themselves. After a brief example of what space weather deflections look like, transmissions sent over a whole year are studied to determine how deflections depend on radio frequency, time of day, and time of year. Then, the effects these deflections have on other signal properties is studied. It is found that deflections are very common at high latitudes, especially in the winter. Deflections tend to increase the travel time of signals, change their frequency, and reduce their signal strength. These results are shown to be connected to polar cap patches and arcs; which are common space weather phenomena near the poles.

1. Introduction

High frequency (HF) radio waves are frequently used for communications, surveillance, and ionospheric research at high latitudes. The deflection of HF radio waves to off-great circle paths can be problematic for these technologies. Reception of the same signal from different propagation paths can lead to multipath errors, degrading received signal quality. Off-great circle propagation is an important consideration for Over-the-Horizon Radars (OTHRs), which use HF radio frequencies for long-range surveillance (Riddolls, 2006; Thayaparan et al., 2018). OTHR require detailed knowledge of the propagation paths available to reach a surveillance target, and the deflection of signals to off-great circle paths can lead to significant errors locating these targets.

HF radio waves can be deflected to off-great circle paths by horizontal gradients in ionospheric electron density. Early research focused on systematic deflections of radio waves caused by the solar terminator. Ross and Bramley (1947) reported deflections of up to 20° near sunrise for an approximately 400 km north-south HF radio link. These systematic deflections were periodically reported on in the latter half of the 20th century (e.g., Burtnyk

© 2024 His Majesty the King in Right of Canada and The Authors. Reproduced with the permission of the Minister of Natural Resources Canada.

This is an open access article under the terms of the [Creative Commons Attribution-NonCommercial-NoDerivs License](https://creativecommons.org/licenses/by/4.0/), which permits use and distribution in any medium, provided the original work is properly cited, the use is non-commercial and no modifications or adaptations are made.

et al., 1962; Morgan, 1974; Tedd et al., 1985). In these studies, the horizontal electron density gradients causing the deflections were frequently characterized as a wrinkling, or tilting of the ionosphere. More recently, focus has shifted to larger deflections caused by localized ionospheric electron density structures, rather than systematic ionospheric tilts. Warrington et al. (1997) reported azimuthal deflections of up to 100° from the great circle direction for HF transmitter links between a transmitter in Alert, Canada, and receivers in Thule, Greenland; Halifax, Canada; and Iqaluit, Canada. These deflections took the form of repeated, monotonic “swings” about the expected azimuthal angle of arrival. They were attributed to reflections off of polar cap density structures, such as polar cap patches and polar cap arcs, and were shown to be consistent with moving reflecting surfaces following ionospheric convection (Warrington et al., 1997).

Polar cap patches are drifting plasma density enhancements found in the polar cap at F-region altitudes (Hosokawa et al., 2019, and references therein) typically when the z-component of the interplanetary magnetic field (IMF B_z) is negative. Patches are operationally defined to have peak electron densities that are twice the background density (Crowley, 1996), range from 100 to 1,000 km in diameter (Coley & Heelis, 1995), come in a variety of shapes, and appear most often during local winter in the Northern Hemisphere (Chartier et al., 2018; Coley & Heelis, 1998; Noja et al., 2013; Spicher et al., 2017). Patches generally drift anti-sunward across the polar cap with ionospheric convection, though non-zero IMF B_y is also known to result in dawn-dusk motion. A statistical study of drift speeds showed that patch drift speeds range up to 500 km/s (Hosokawa et al., 2009), however, faster speeds have been measured (e.g., Weber et al., 1984). Patches were first detected with ionosondes by Meek (1949), though they were not studied frequently until Weber and Buchau (1981) observed patches with all-sky imagers. They have also been investigated with in-situ measurements (e.g., Goodwin et al., 2015; Kivanç & Heelis, 1997; Spicher et al., 2015) and incoherent scatter radars (e.g., Dahlgren et al., 2012; Jin et al., 2019; Oksavik et al., 2006; Perry & St.-Maurice, 2018).

Polar cap arcs are a kind of sun-aligned auroral arc that appear in the polar cap mainly during times of positive IMF B_z (Berkey et al., 1976; Hosokawa et al., 2020; Valladares et al., 1994). They can appear anywhere in the polar cap with a variety of lengths and intensities, sometimes even stretching across the entire polar cap. Typically, larger and brighter arcs are referred to as “transpolar” arcs, while smaller scale, dimmer arcs are called “sun aligned” arcs (Hosokawa et al., 2020). Polar cap arcs predominately form in the evening sector when IMF $B_y > 0$, and in the morning sector when IMF $B_y < 0$ (Fear & Milan, 2012). Once formed, they tend to move toward dusk when IMF $B_y > 0$, and toward dawn when IMF $B_y < 0$ at speeds of a few hundred m/s (Hosokawa et al., 2011; Valladares et al., 1994). As auroral arcs are comprised of precipitating energetic particles, they are also associated with ionospheric electron density enhancements. Some global navigation satellite system (GNSS) total electron content (TEC) measurements of polar cap arcs showed increased electron densities equivalent to up to 7 MHz in critical frequency (Jayachandran, Hosokawa, et al., 2009; Jayachandran et al., 2012). The height of the bottom of these electron density enhancements were seen at altitudes ranging from 110 to 300 km, likely depending on the energy of the precipitating particles.

HF radio wave deflection by polar cap ionospheric density structures is an important consideration for radio propagation models. Warrington (1998) compared an entirely polar cap propagation path to one in which the reflection point was in the auroral zone. They found the polar cap path resulted in much greater azimuthal deviations ($\sim 35^\circ$) than the auroral zone path ($\sim 2.5^\circ$). Stocker et al. (2013) showed that Doppler spreads for polar cap propagation paths were significantly larger than those measured for sub-auroral paths. Ray tracing methods have been used to better understand how polar cap patches divert HF radio waves to off-great circle paths. For example, Zaalov et al. (2003) compared measurements of off-great circle propagation due to polar cap patches and arcs to ray tracing simulations of propagation through a model ionosphere with added model patches and arcs. They found the simulations were able to reproduce the character of the observations, suggesting that ray traces could be used to investigate propagation where observations are not available. The development of the ray tracing model, as well as the model ionosphere and patches is further explained in Zaalov et al. (2005). Warrington et al. (2012) presented coverage estimates for high latitude HF radio propagation derived from ray tracing simulations, including how the presence of polar cap patches affects HF radio coverage. OTHR sensitivity to electron density structures has also led to research on how polar cap electron density enhancements could affect OTHR operation. Thayaparan et al. (2020, 2021) used an improved version of the model presented in Zaalov et al. (2005) to demonstrate how polar cap patches could lead to dramatic changes in expected OTHR coverage and ground range.

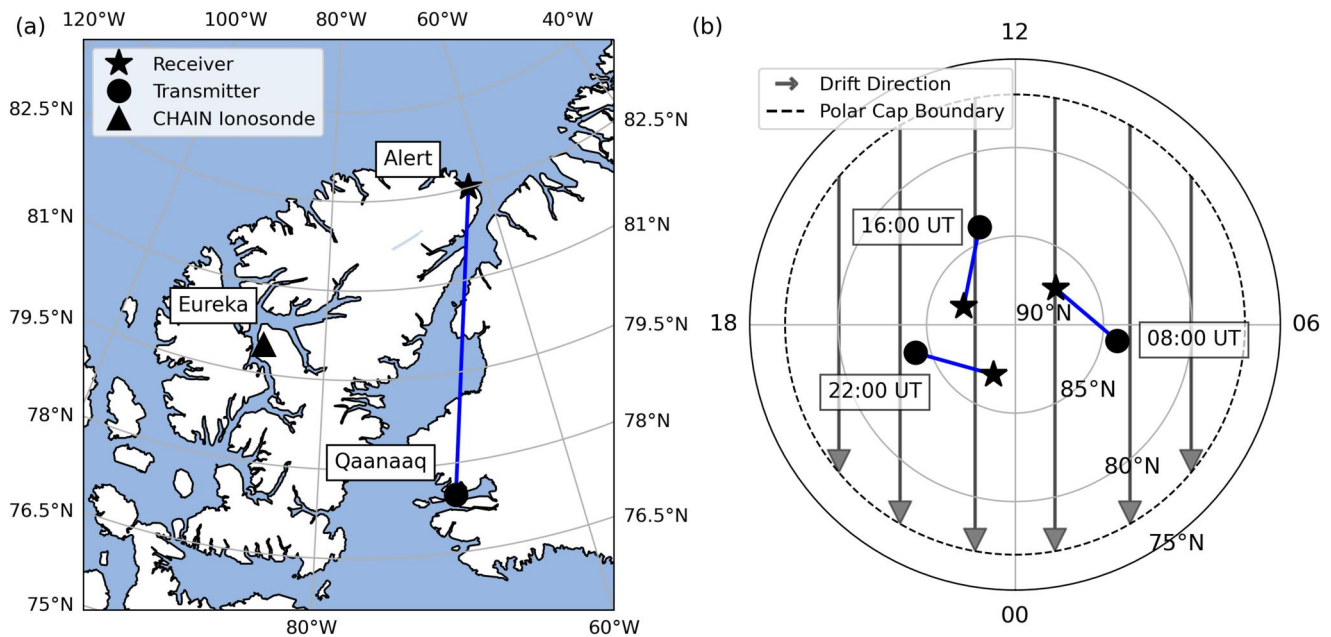


Figure 1. (a) Map showing the geographic location of the Qaanaaq HF transmitter, Alert HF receiver, and Eureka CHAIN ionosonde in an orthographic projection. (b) Map in geomagnetic latitude and magnetic local time (MLT) coordinates showing the location and orientation of the Qaanaaq to Alert HF radio link at 08:00, 16:00, and 22:00 UT on 07 Nov 2013 relative to the polar cap boundary (set to 77° magnetic latitude), and to a theoretical anti-sunward, polar cap flow pattern representative of B_z -negative, two-cell ionospheric convection.

While previous work shows examples of patch-affected propagation, and quantified the magnitude of possible deviations from the great-circle path, a comprehensive study of off-great circle propagation in the polar cap has not been performed. In this study, nearly 2.5 years of data taken between 2012 and 2016 from a polar cap HF radio link are used to evaluate both the occurrence of off-great circle propagation in the polar cap, and how off-great circle propagation affects HF radio signal properties. Section 2 describes the instrumentation and data. Section 3 presents an example of off-great circle propagation caused by polar cap patches occurring over a typical day. This is meant to establish that these deflections are due to polar cap ionospheric density structures, and show how deflections and other signal parameters vary with time. A statistical analysis of the HF radio link data set is performed in Section 4. The occurrence of off-great circle propagation is explored overall, in terms of time of day and time of year. The dependence of other HF radio signal parameters on deflection from the great circle is explored. Section 5 discusses how these results relate to HF radio interactions with polar cap patches and arcs, and possible implications for HF radio technologies in the polar cap.

2. Instrumentation and Data

This study uses data from a 577 km HF radio link consisting of a transmitter located in Qaanaaq, Greenland (77.47°N, 69.23°W; QAN) and a receiver located in Alert, Nunavut (82.50°N, 62.35°W; ALE). Qaanaaq and Alert are both located in the polar cap, making this link especially useful for investigating the effects of polar cap ionospheric phenomena on HF radio signals. The Qaanaaq transmitter operated at 100 W and utilized an end-fed V antenna (<https://www.bwantennas.com/acs.html>) with a directional gain of 0 dB for transmissions. The Alert receiver consists of an array of elevated feed vertical monopoles, connected to an 8 channel direction finding receiver, and is now part of the Natural Resources Canada (NRCAN) HF radio network (Cameron et al., 2021). Figure 1a shows the location (in geographic coordinates) of the HF radio link relative to the Eureka Canadian High Arctic Ionospheric Network (CHAIN) ionosonde used in the following section. Figure 1b shows the location and orientation of the HF radio link at 08:00, 16:00, and 22:00 UT on 07 Nov 2013 relative to the polar cap boundary and a typical anti-sunward, B_z -negative flow pattern in geomagnetic coordinates. The anti-sunward flow pattern shown is intended to be illustrative tool, and is not derived from specific measurements or models.

The QAN transmitter operated by sending 2 s long, GNSS time-synchronized signals at each of six distinct frequencies multiple times an hour according to a prearranged schedule. Each transmission was a repeating 13-bit

Barker coded signal, which was chosen to be easily identifiable from background noise. The ALE receiver listened for and recorded matching Barker coded signals at the correct frequencies according to the same schedule. Signals were recorded with a bandwidth of 50 kHz, and filtered down to 3 kHz before processing. For each detected transmission, signal parameters including signal-to-noise ratio (SNR), time of flight (TOF), Doppler shift, and Doppler spread were calculated and recorded.

The presence of ionospheric electron density structures in the polar cap make it a complicated propagation environment for HF radio waves. HF radio waves often arrive at the receiver from a multitude of different propagation paths, making it difficult to determine a single set of signal parameters. Accordingly, signal parameters such as the TOF and Doppler shift corresponding to the highest received signal power were calculated and recorded for each transmitted signal. Elevation and azimuthal angle of arrival information were calculated with a direction finding algorithm that compared signal characteristics detected by different antenna elements. Often for low SNR signals, the received signal power is weak enough that the algorithms responsible for calculating signal parameters become dominated by noise, leading to erroneous signal parameters being recorded. This is most common for azimuthal and elevation angle of arrival measurements. In order to minimize the prevalence of erroneous angle of arrival measurements, only signals with SNRs > 0 dB were considered in this study.

This study considers data recorded by the QAN–ALE link between June 2012 and August 2016. There were some periods of non-operation during this time due to the remote locations of both the transmitter and receiver. The most notable gap is between October 2014 and February 2016. Factoring in these periods, the link was operational for 855 days total. The set of frequencies signals were transmitted at, and their accompanying transmission rates changed on 15 December 2013 to accommodate other transmitters. From June 2012 to 15 December 2013, 4.6374, 6.9544, 8.0081, 10.3914, 11.1184, and 14.3644 MHz signals were each transmitted at 30 signals per hour. After 15 December 2013, the 10.3914 MHz transmissions were replaced with 18.3814 MHz transmissions, and transmission rates were reduced to accommodate other transmitters such that 4.6374, 6.9544, 8.0081, 11.1184, 14.3644, and 18.3814 MHz signals were sent at rates of 4, 8, 24, 24, 24, and 8 signals per hour, respectively. For the rest of this study, frequencies are written rounded to one decimal place for brevity. 18.4 MHz signals rarely reached ALE at all, and are not considered in this study. Unfiltered QAN–ALE data recorded from 2012 to 2016 (including SNR < 0 dB and 18.4 MHz signals) can be found at the Harvard Dataverse (<https://doi.org/10.7910/DVN/RGDNRI>).

3. Example of Off-Great Circle Propagation

This section showcases an example of off-great circle propagation caused by polar cap patches, and the effect on received signal parameters. 07 November 2013 was selected as an illustrative example of off-great circle propagation due to signatures in the HF data of polar cap patches crossing the propagation path. Figure 2 shows (a) IMF B_z timeshifted to the magnetopause, (b) the auroral electrojet (AE) index, and the frequency of the F2 layer of the ionosphere (foF2) measured by an ionosonde in (c) Eureka for 07 November 2013. The location of the Eureka ionosonde relative to QAN and ALE is shown in Figure 1. Two horizontal blue lines below the x -axis indicate times in which IMF B_z was negative. IMF B_z and AE index data was obtained from the OMNI data set (King, 2005; King & Papitashvili, 2020), while Eureka ionosonde data came from CHAIN (Jayachandran, Langley, et al., 2009).

Interplanetary and ionospheric conditions seen throughout the day suggest the presence of polar cap patches. IMF B_z (Figure 2a) is primarily negative for the first half of the day, reaching -12.5 nT before transitioning to positive at approximately 12:00 UT, and remains positive until 19:00 UT, after which it fluctuates between 0 and -5 nT for the rest of the day. The AE index (Figure 2b), which is a measure of geomagnetic activity in the auroral zone, is elevated during the periods of negative IMF B_z . Polar cap patches are known to appear at times when geomagnetic activity is occurring (Hosokawa et al., 2019).

The foF2 measured in Eureka (Figure 2c) varies substantially across the day. The ionosonde measures repeated, 10s of minutes long fluctuations in foF2 concurrent with the periods of negative IMF B_z and elevated AE index. These fluctuations range between 4 and 8.8 MHz during the first period of negative IMF B_z , and between 3.6 and 7.6 MHz during the second period. These foF2 fluctuations are consistent with polar cap patches passing over the Eureka ionosonde. The ionospheric electron density during these fluctuations reaches more than twice the background density, consistent with the formal definition of a polar cap patch (Crowley, 1996).

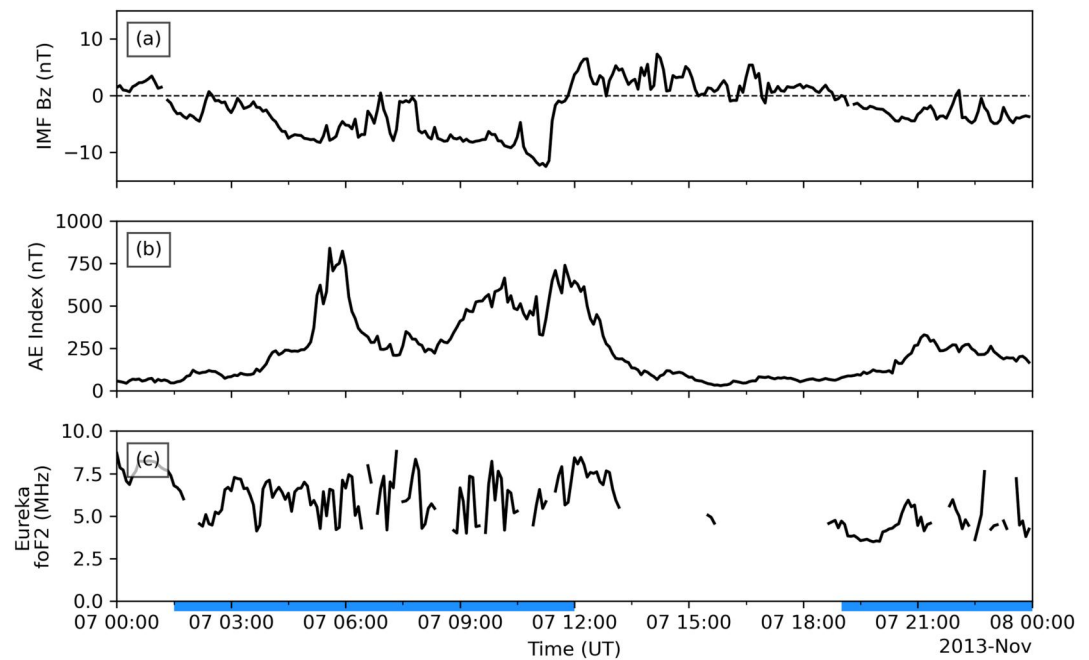


Figure 2. Summary plot of relevant interplanetary and ionospheric conditions for 07 November 2013. Panels show (a) IMF B_z , (b) AE index, and (c) foF2 measured by a Canadian High Arctic Ionospheric Network (CHAIN) ionosonde in Eureka. Two periods during which IMF B_z was negative are indicated with horizontal blue lines below the x -axis.

Figure 3 shows a selection of recorded parameters for all signals received by the Alert HF radio receiver on 07 November 2013. The panels on the left (a–e) show time series of (a) signal frequency (b) azimuthal angle of arrival, (c) TOF, (d) Doppler shift, and (e) Doppler spread across the entire day. The two periods of negative IMF B_z are indicated by horizontal blue lines below the x -axis. The panels on the right (f–j) show a zoomed-in view of the same signal parameters for 22:30–23:30 UT, intended to illustrate a single patch crossing. This time is indicated with a red horizontal line below the x -axis. Throughout the day, all frequencies except 14.4 MHz arrive consistently at Alert (Figure 3a), apart from a period between 14:00 and 20:00 UT, in which reception for 10.4 and 11.1 MHz signals becomes intermittent. This time corresponds to a period of low geomagnetic activity (indicated by IMF B_z and AE in Figure 2), and consequently low polar cap patch occurrence. This suggests that polar cap patches aided in the reception of 10.4 and 11.1 MHz waves outside this period, and that the background ionospheric electron density was too low to consistently reflect these frequencies back toward Alert without the patches.

The great circle heading (GCH) from Alert to Qaanaaq is an azimuthal angle of 196.79° . Deviations from this value indicate off-great circle propagation. During the first period of negative IMF B_z (01:30–12:00 UT), the received azimuth of radio signals at all received frequencies (Figure 3b) undergoes repeated “swings,” in which the azimuth repeatedly changes from below the GCH to above the GCH. The azimuthal extent of these swings varies by frequency, such that higher frequencies exhibit larger deflections. Deflections of $>90^\circ$ from the expected great circle azimuth are observed for the higher frequencies, consistent with previous observations of azimuthal deflections thought to be caused by polar cap patches crossing the propagation path (e.g., Warrington et al., 1997; Zaalov et al., 2003). Additionally, the higher frequency signals (10.4 and 11.1 MHz) during this period are only detected at large deflection angles from the GCH. This is probably because these signals are at too high of a frequency to be reflected back to Alert along the great circle. This is consistent with the relative absence of 10.4 and 11.1 MHz signals during the subsequent B_z -positive period from 12:00–19:00 UT. They can only reach Alert along propagation paths with large azimuthal deflections, since these paths interact with the ionosphere and patches at shallower elevation angles.

The swings in azimuth end at 12:00 UT, consistent with IMF B_z transitioning to positive. Geomagnetic activity indicated by the AE index and fluctuations in foF2 also cease soon after. Between 12:00 and 19:00 UT, a large, unstructured spread in azimuthal angle of arrival can be seen at all frequencies. After IMF B_z becomes negative

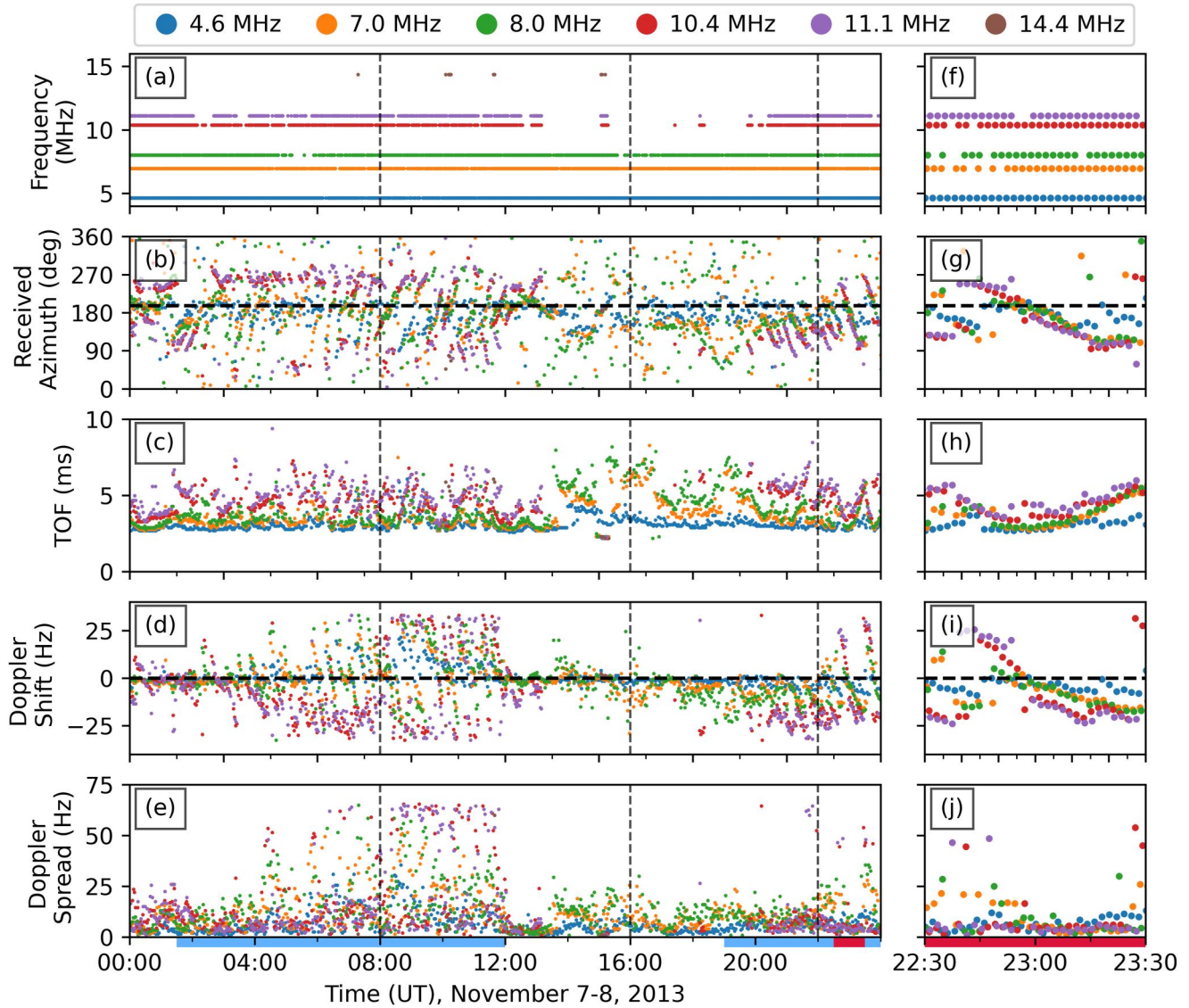


Figure 3. Summary plot of HF radio signals for the Qaanaaq to Alert propagation path on 07 November 2013. Panels (a–e) from the top-down show (a) Periods of HF reception of signals at the prescribed frequency, (b) azimuthal angle of arrival, (c) time of flight (TOF), (d) Doppler shift, and (e) Doppler spread across the entire day. Panels (f–j) show a zoomed in view of the same signal parameters from 22:30–23:30 UT. Frequencies recorded are: 4.6 MHz (blue), 7.0 MHz (orange), 8.0 MHz (green), 10.4 MHz (red), 11.1 MHz (purple), 14.4 MHz (brown). Time is indicated by day of month and HH:MM on the bottom x-axis, with the month and year indicated in the lower right. The dashed horizontal lines in (b, g) indicate the great circle heading (GCH) from Alert to Qaanaaq. Three vertical dashed lines in panels (a–e) indicate times the orientation of the HF link was shown in the right panel of Figure 1. Two periods of negative IMF B_z are indicated with horizontal blue lines, and the zoomed-in period shown in panels (f–j) is indicated by a horizontal red line below the x-axis.

again at 19:00 UT, the azimuthal angle of arrival exhibits azimuthal swings transitioning from approximately the GCH to $\sim 100^\circ$ below the GCH. Figure 3g shows a zoomed in view of a single, especially coherent azimuthal swing likely associated with a polar cap patch. The azimuthal angle of arrival for each received frequency follows the same general curve, varying from above the GCH to below the GCH over the hour, though azimuths measured at the same time for different frequencies do differ by up to 30° at times. This is likely the result of different frequencies reflecting off different parts of the patch, since higher frequencies will penetrate farther.

Other signal parameters exhibit distinct behavior during the two negative IMF B_z periods. During both periods, the TOF at all frequencies (Figure 3c) undergoes repeated rises and falls between 2.2 and 6.8 ms that line up with the swings in angle of arrival, such that signals with the largest azimuthal deflections from the GCH also have the highest TOFs. This is not surprising since signals that experience larger azimuthal directions likely also take

longer paths to reach Alert. Correspondingly, higher frequencies generally reach larger TOFs, since they also experience larger deflections. The TOFs for all frequencies seen in Figure 3h are largest at the beginning and end of the crossing. The TOFs for individual frequencies are clearly stratified according to frequency as well. Referring back to the full interval, from 12:00–19:00 UT when IMF B_z is positive, the TOF at all frequencies undergoes slower and large variations. During this time signals are received with TOFs of up to 8.0 ms, larger than what is seen when IMF B_z is negative.

Doppler shifts (Figure 3d) also exhibit “swings” that correspond to swings in azimuthal angle of arrival during the two negative IMF B_z periods. During the first period (01:30–12:00 UT), Doppler shifts repeatedly change from as high as ~ 30 Hz to as low as ~ -25 Hz. Higher frequency signals generally experience larger positive and negative Doppler shifts. During the second period of negative IMF B_z (18:00–24:00 UT), repeated swings in Doppler shift from 0 Hz to as low as -30 Hz can be seen concurrent with azimuthal angle of arrival swings. Notably, while the azimuthal angle of arrival swings reverse direction between the first and second negative IMF B_z periods, the accompanying Doppler shifts do not. Doppler shifts at all frequencies for the single patch crossing (Figure 3i) drop from above to below zero Hz across the interval, lining up with the azimuthal swing. However, swings for different frequencies do not line up. Instead, the slope of the swings in Doppler shift get larger with increasing frequency.

Doppler spread (Figure 3e) is a measure of the size of the range of Doppler shifts a given HF radio signal was received at. Doppler spread for all frequencies varies between 0 and 20 Hz from 00:00 UT until midway into the first negative IMF B_z period at 04:30 UT. At 04:30 to 12:00 UT, larger variations in Doppler spread of up to 65 Hz can be seen at all frequencies. 04:30 UT is approximately the time when the AE index (Figure 2b) becomes elevated past 250 nT. For the rest of the day, Doppler spread varies again between 0 and 20 Hz at all frequencies. There is a small population of isolated 10.4 and 11.1 MHz signals with Doppler spreads between 45 and 65 Hz during the second period of negative IMF B_z . Doppler spreads measured for the single, clear patch crossing during this period (Figure 3j) are generally low. This contrasts with the increased Doppler spreads seen for other patch crossings. It could be that the patch responsible for the swing from 22:30–23:30 UT contained less internal structuring. Simpler internal structuring would result in smaller Doppler spreads since there would be less variation in the Doppler shift experienced by a single transmission. It is also consistent with the reduced scatter in azimuthal angle of arrival compared to the first interval, since a spatially simpler patch would reflect HF radio waves in a more consistent way.

4. Statistical Analysis

4.1. Occurrence and Magnitude of Off-Great Circle Deflections

A complete year of Qaanaaq to Alert transmissions from April 2013 to April 2014 was used to study the occurrence and magnitude of off-great circle propagation in the polar cap. This period represents the most consistent 1-year interval of data collection, allowing examination of the data without seasonal bias. It should be noted that this period occurred during solar maximum, and therefore observes higher geomagnetic activity, and is expected to observe a higher occurrence of polar cap density structures than in surrounding years. Additionally, the data only represents transmitted signals that actually reached and were detected by the receiver. This does not include signals that experienced too much absorption to reach Alert, signals that escaped to space, or signals that never reached the receiver due to azimuthal deflections.

Figure 4 shows normalized histograms with 2° bins representing the distribution of deflections from the GCH for all received QAN–ALE HF radio signals from 01 April 2013 to 01 April 2014. Since the transmission rates for all frequencies changed in December 2013, deflections were weighted by the inverse of the transmission rate to ensure all parts of the year were represented equally in time. The histograms were also normalized to ensure the sum across all bins is 1. From the top down, panels show distributions for (a) 4.6 MHz, (b) 7.0 MHz, (c) 8.0 MHz, (d) 11.1 MHz, and (e) 14.4 MHz. The distribution for 10.4 MHz is omitted since the frequency was not transmitted for the entire year. The vertical axis range cuts off the strong peak observed in all distributions at 0° deflection to emphasize the features away from the great-circle heading. All distributions show significant populations of deflections that are distinct from the peak at 0° . The distribution for 4.6 MHz has a distinct population that peaks at -22° deflection. Distributions for frequencies >4.6 MHz contain sizable populations of positive and negative deflections, that increase in relative size with increasing frequency up to 11.1 MHz. The distribution for 14.4 MHz contains a smaller sized population of deflections ($>30^\circ$) compared to 11.1 MHz. Since

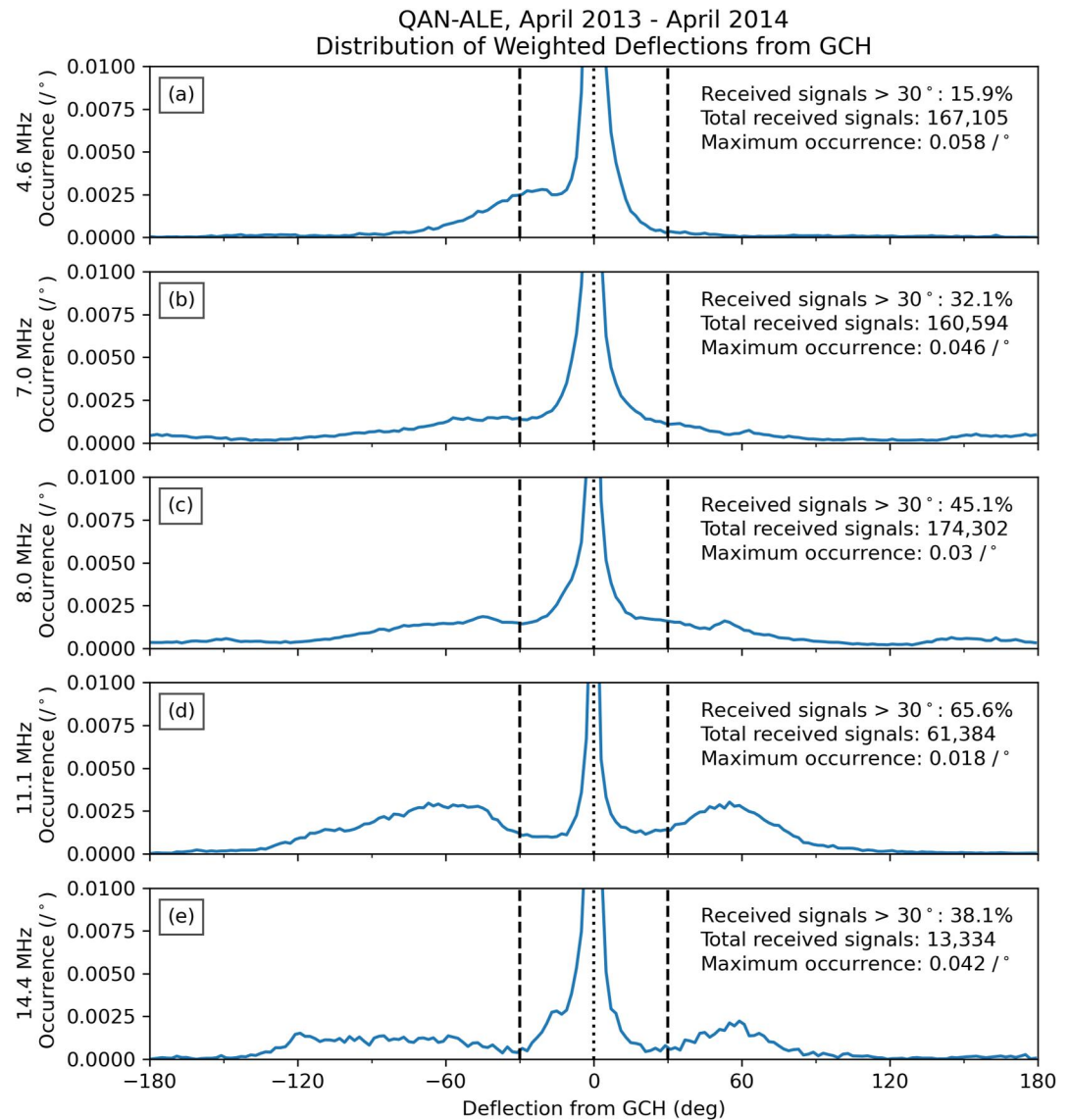


Figure 4. Normalized distributions of deflection from the great circle heading for all signals received at Alert from Qaanaaq from 01 April 2013–01 April 2014. Panels show distributions for (a) 4.6 MHz, (b) 7.0 MHz, (c) 8.0 MHz, (d) 11.1 MHz, (e) 14.4 MHz. Vertical dashed lines in each panel indicate $\pm 30^\circ$, and the vertical dotted line indicates 0° . The y-axis range in each panel was chosen to focus on the distribution away from the great circle heading. The percentage of received signals with deflections $> 30^\circ$, the total number of signals received, and the peak distribution density are reported in the top right of each panel. Deflections were weighted by the inverse of transmission rate to ensure all parts of the year were represented equally.

considerably fewer signals were received at 14.4 MHz compared to the other frequencies, some discrepancies at 14.4 MHz may be due to the smaller sample size.

At the higher frequencies, these populations of deflections have distinct positive and negative peaks. For example, the distribution for 11.1 MHz (panel d) has localized west and east peaks at approximately -70° and 60° from the GCH. At frequencies ≥ 11.1 MHz, there are local minima at approximately $\pm 30^\circ$ deflection, where the decreasing on-great circle population meets the increasing off-great circle population. This minimum can also be seen for negative deflections in the 8.0 MHz distribution. Dashed vertical lines at $\pm 30^\circ$ show this transition point in each panel. On average over the year, received 4.6, 7.0, 8.0, 11.1, and 14.4 MHz signals had deflections larger than 30° 15.9%, 32.1%, 45.1%, 65.6%, and 38.1% of the time, respectively. These distributions are also asymmetric. More signals arrive with negative deflections than positive deflections for all frequencies, which corresponds to more

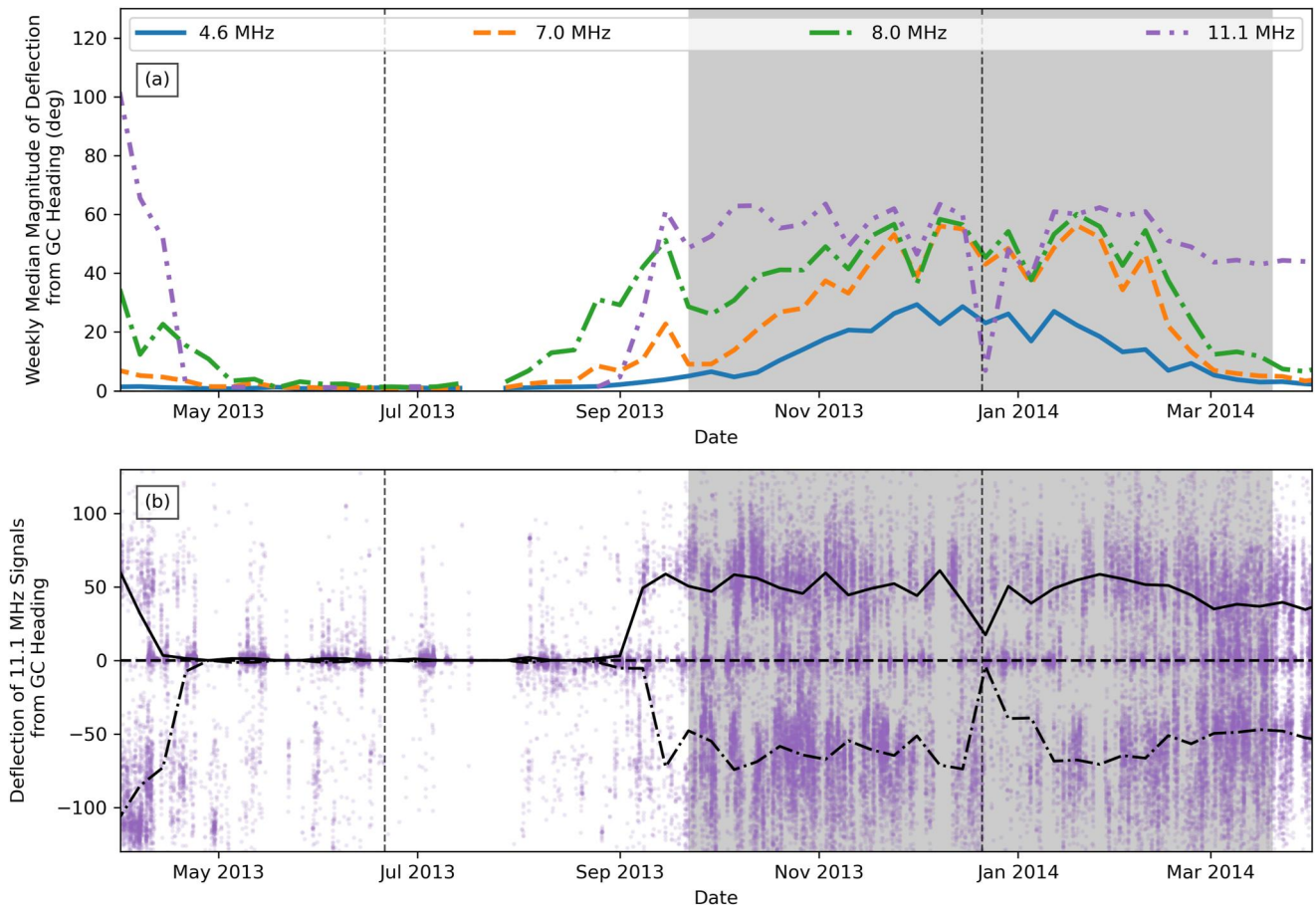


Figure 5. (a) Weekly median magnitude of deflection of HF radio signals from 01 April 2013–01 April 2014 for (blue) 4.6, (orange) 7.0, (green) 8.0, and (purple) 11.1 MHz signals. Frequencies are also distinguished by line style. Vertical dashed lines indicate winter and summer solstices. The shaded region indicates local winter. (b) Scatter plot of deflection from the GCH versus time for 11.1 MHz signals received from 01 April 2013–01 April 2014. Individual signals are indicated with purple, semi-transparent points. The solid and dash-dotted curves show the weekly median deflection for positive and negative deflections respectively.

signals arriving from east of the great circle heading than west. Again averaged over the year, received 4.6, 7.0, 8.0, 11.1, and 14.4 MHz signals arrived from the east of the GCH 61.2%, 59.8%, 56.6%, 55.9%, and 58.5% of the time, respectively.

These results were determined from an analysis of individually received signals and their accompanying deflections. However, for operation of HF radio technology at high latitudes, it may be more useful to understand what percentage of transmitted signals can be expected to be deflected to off-great circle paths, rather than the percentage of received signals. To do this, the number of hour-long intervals in which the median magnitude of deflection from the GCH was larger than 30° was compared to the total number of intervals for which the QAN–ALE link was operational. The percentage of intervals where the median deflection was $>30^\circ$ was 11.8%, 29.1%, 43.1%, 36.1%, and 9.6% for the 4.6, 7.0, 8.0, 11.1, and 14.4 MHz frequencies, respectively, for the April 2013 to April 2014 period considered. The drop in percentage for the higher frequencies is due to the much lower number of signals received compared to the lower frequencies. Due to the short length of the QAN–ALE path, high frequency signals are more likely to escape to space.

Since the occurrence of polar cap density enhancements thought to be responsible for signal deflections vary significantly with season and time of day, it is useful to explore how deflections from the GCH also vary with time. To investigate how the magnitude of off-great circle deflections changed over the year, the median magnitude of deflection from the GCH was calculated for signals received during each week from 01 April 2013–01 April 2014, for each frequency. Week-long bins were chosen to smooth out day-to-day variability caused by changing geomagnetic activity, while still preserving variation on longer time scales. Figure 5a shows this weekly

median deflection for (blue) 4.6, (orange) 7.0, (green) 8.0, and (purple) 11.1 MHz. 14.4 MHz signals were omitted because too few signals were received per week to calculate consistent weekly medians. Weeks for which less than 10% of transmitted signals were received were also omitted on a per-frequency basis for the same reason. The shaded region in the figure indicates local winter (between the fall and spring equinoxes).

The median weekly deflection for all frequencies reach minimum and maximum values near the summer and winter solstice, respectively. Median weekly deflections for all frequencies during the summer are especially close to zero. Comparing different frequencies, median weekly deflection generally increases with increasing frequency. This relationship can be seen throughout the year, though the median daily deflection for 7.0, 8.0, and 11.1 MHz reaches a consistent maximum near the winter solstice. Median daily deflection reaches $\sim 30^\circ$ on average for 4.6 MHz, and $\sim 50^\circ$ on average for 7.0, 8.0, and 11.1 MHz in the winter months. During the first week of 2014, the weekly median deflection for 11.1 MHz temporarily drops to close to zero.

Figure 5b shows a scatter plot of individual deflections experienced by 11.1 MHz signals across the same time period as panel (a). Overlaid are weekly medians for just positive and negative 11.1 MHz deflections. Comparing the individual deflections to the medians, changes in the weekly median deflection seem to be due to changes in the occurrence of large deflections compared to on-great circle signals, rather than changes in the magnitude of the off-great circle deflections. During the summer, the occurrence of 11.1 MHz off-great circle deflections is close to zero, while large deflections are extremely common in the winter. The occurrence of received 11.1 MHz signals is lower near the winter solstice, likely because polar cap ionospheric electron density is consistently low at the time due to the lack of solar photoionization.

To investigate how deflections from the GCH varied across the day, received signals were binned by time of day (UT) in 2-hr increments and day of year in 21-day increments, and the median magnitude of deflection from the GCH was calculated for each bin from 01 April 2013 to 01 April 2014. As with Figure 5, bin sizes were chosen to ensure enough signals fell in each bin to calculate consistent medians while still showing changes across the day and year.

Figure 6 shows the median magnitude of deflection from the GCH versus time of day and day of year for (a) 4.6, (b) 7.0, (c) 8.0, (d) 11.1, and (e) 14.4 MHz signals. The solstices and equinoxes are marked with solid and dashed white vertical lines, respectively. The majority of deflections for all frequencies occur in local winter. How median deflection varies across the day clearly changes with both frequency and time of year. During the winter months, for the lower three frequencies, the median magnitude of deflection peaks in the UT morning, and the duration of the day for which large deflections occur gets wider with increasing frequency. For instance, the median magnitude of deflection is $>45^\circ$ from 10:00 to 12:00 UT for 4.6 MHz, from 00:00–16:00 UT for 7.0 MHz, and from 00:00–18:00 UT and 22:00–24:00 UT for 8.0 MHz. During summer months only the 8.0 MHz signal experiences significant deflections, with a peak at ~ 06 UT.

The distribution of median deflection with respect to time of day and day of year for the two higher frequencies is noisy due to the relatively lower number of received signals, especially 14.4 MHz. However, there are clear differences in the variation of median deflection across the day when compared to the lower frequencies. Focusing on 11.1 MHz, median deflection near the beginning and end of local winter is high across the day and largest in the morning, matching the lower frequencies. Near the winter solstice however (from roughly mid-November to mid-January), the median magnitude of deflection is close to zero from 02:00 and 14:00 UT, and almost entirely $>50^\circ$ after 14:00 UT and before 02:00 UT. While there is more noise due to the lower number of received signals, the median deflection distribution for 14.4 MHz signals generally agrees with the pattern for 11.1 MHz, except that large deflections are only detected from 18:00–22:00 UT near the winter solstice.

4.2. Effects of Off-Great Circle Propagation on HF Radio Signal Parameters

This section examines how off-great circle propagation affects other relevant HF radio signal characteristics. From the set of all signals received during local winter (between the fall and spring equinoxes) between June 2012 and August 2016, 2D histograms of signal deflections from the GCH and a selection of relevant HF radio properties for each of six frequencies (4.6, 7.0, 8.0, 10.4, 11.1, and 14.4 MHz) were generated. The counts in these histograms were converted to 2D discrete distribution densities so that the sum over all bins, multiplied by the bin widths would be 1. To focus on off-great circle signals, which were shown in Figure 5 to be much more common in winter, only local winter signals were considered.

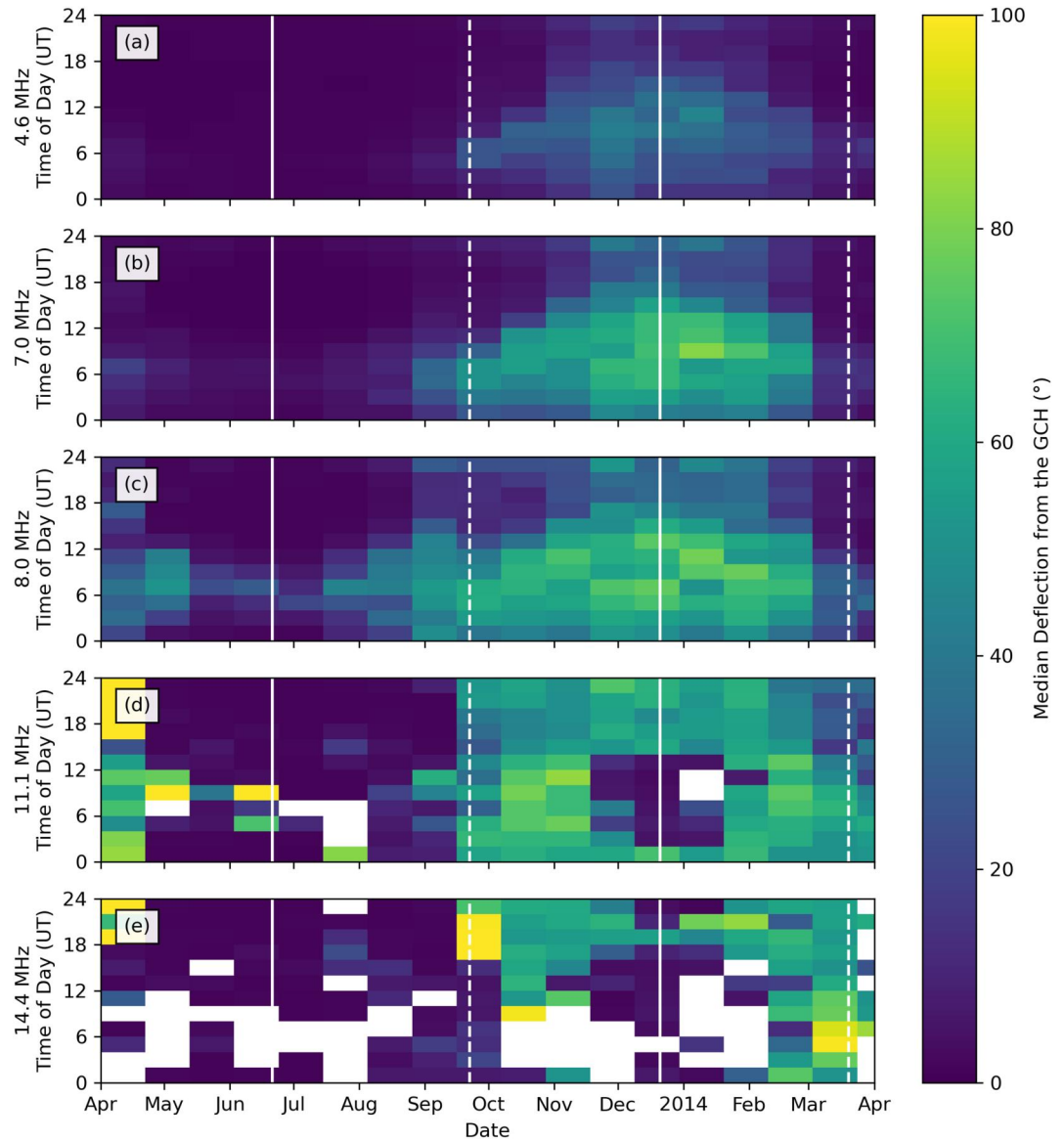


Figure 6. Median magnitude of deflection from the GCH from 01 April 2013–01 April 2014 for HF radio signals binned by time of day (UT) in 2-hr increments and day of year in 21 days increments for (a) 4.6, (b) 7.0, (c) 8.0, (d) 11.1, and (e) 14.4 MHz signals. Medians were not calculated for bins containing <10 received signals, and those bins are marked white. Solid white lines indicate the winter and summer solstices and dashed white lines indicate the spring and fall equinoxes.

Figure 7 shows the discrete distribution density of local winter signals versus TOF (0.2 ms bins) and deflection from the GCH (8° bins) for (a) 4.6, (b) 7.0, (c) 8.0, (d) 10.4, (e) 11.1, and (f) 14.4 MHz. The range of TOFs seen for all frequencies has a hard cutoff which is consistent with the 1.91 ms on-great circle speed of light travel time between QAN and ALE. The range of signal deflections extends from -180° to 180° . All frequencies show two distinct populations. Closest to the 1.91 ms lower cutoff, there is a population of largely on-great circle signals separated in TOF from the rest of the distribution for all frequencies. This population has a limited extent in deflection that increases with increasing frequency. At the higher frequencies (10.4–14.4 MHz), increasing deflection does lead to a small increase in the TOF. The TOF associated with the peak of this part of the distribution is consistent with the TOF expected for on-great circle propagation from QAN–ALE, with a single reflection off the E region (~ 100 km altitude).

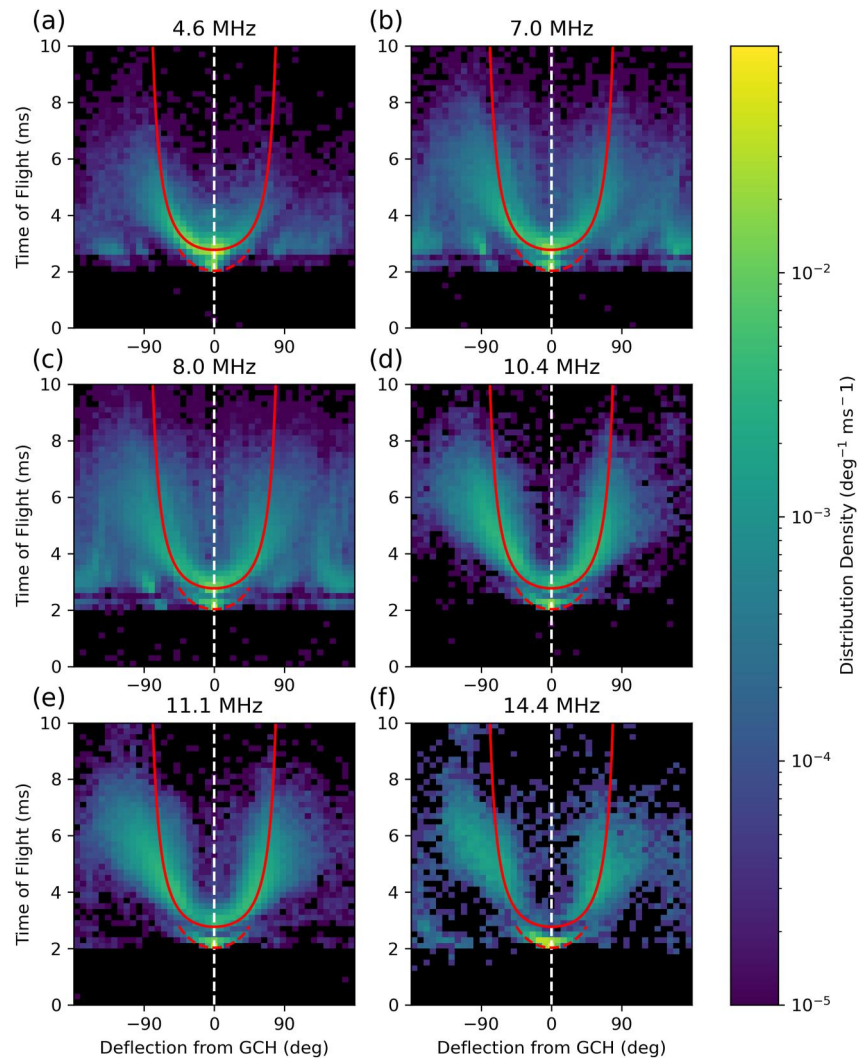


Figure 7. Discrete distribution density of received signals versus time-of-flight and deflection from the great circle heading for (a) 4.6, (b) 7.0, (c) 8.00, (d) 10.4, (e) 11.1, (f) 14.4 MHz. All distributions are plotted with a logarithmic color scale to better highlight off-great circle signals. Only radio signals received during local winter (between fall and spring equinoxes) were considered. Zero deflection is indicated by a vertical white dashed line. The red and light blue overlaid curves show the expected time of flight assuming radio waves reflected off patches crossing halfway between Qaanaaq and Alert at 300 and 100 km altitude respectively.

The rest of the TOF range is represented by a population of signals with TOFs ranging from 2.4 ms to up to 10 ms, with deflections ranging from -180° to 180° . This population is very similar at all frequencies, except for 4.6 MHz, for which the range of TOFs is reduced. At all frequencies, signals with larger deflections tend to also have larger TOFs. The population also shows a spreading in the off-great circle part of the distribution, such that signals with increasingly larger TOFs have a larger range of possible deflections. The TOF associated with the on-great circle part of this population is consistent with on-great circle propagation from QAN–ALE with a single reflection off the F-region (300 km).

Figure 8 shows the discrete distribution density of local winter signals versus Doppler shift (1.5 Hz bins) and deflection from the GCH (8° bins). At all frequencies, the peak distribution density occurs for zero Doppler shift and zero deflection from the GCH. Away from zero deflection, all frequency distributions are largely symmetric with respect to Doppler shift and deflection. All frequencies show a pattern in which larger deflections from the GCH up to 90° yield a larger possible range of positive and negative Doppler shifts. This range also increases with increasing frequency. For deflections larger than $\pm 90^\circ$, the distribution density tapers off such that the largest

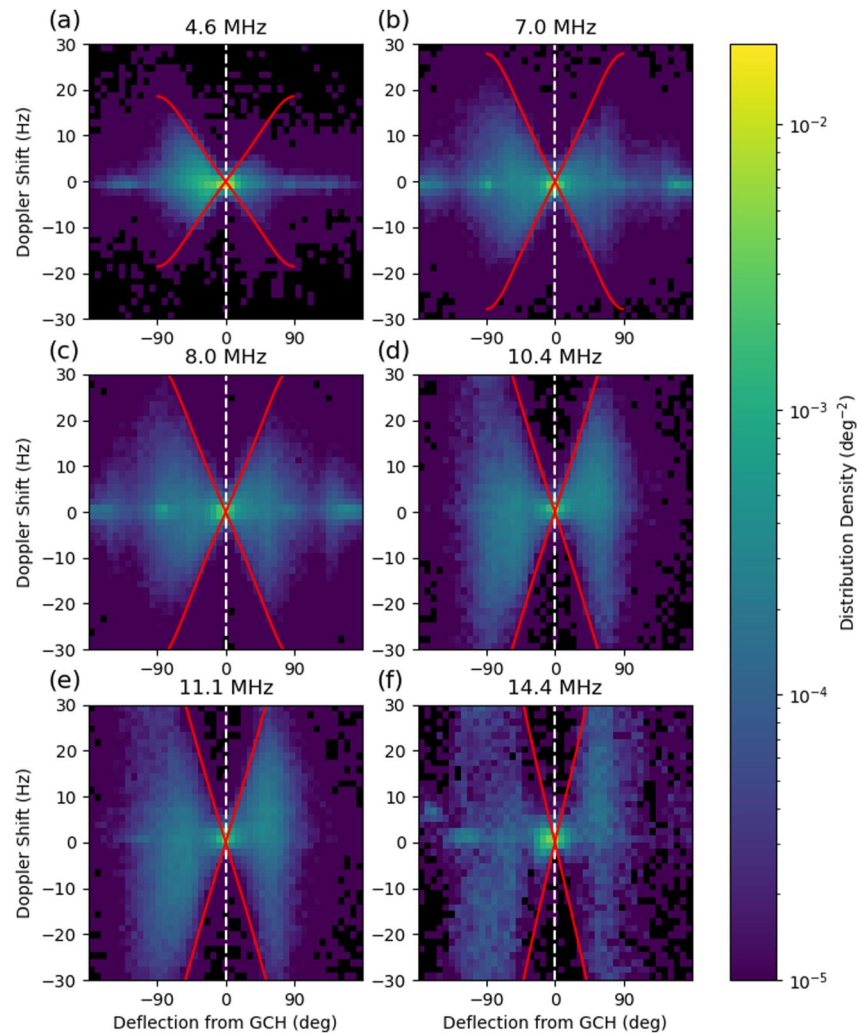


Figure 8. Discrete distribution density of received signals versus Doppler shift and deflection from the great circle heading for (a) 4.6, (b) 7.0, (c) 8.0, (d) 10.4, (e) 11.1, (f) 14.4 MHz. All distributions are plotted with a logarithmic color scale to better highlight off-great circle signals. Only radio signals received during local winter (between fall and spring equinoxes) were counted. Zero deflection is indicated by a vertical white dashed line, and the red overlaid curves show the expected Doppler shift assuming radio waves reflected off patches crossing halfway between Qaanaq and Alert at 300 km altitude.

deflections tend to have Doppler shifts closer to zero. The 4.6 MHz distribution shows an asymmetry in which negative azimuthal deflections lead to a larger range of Doppler shifts than positive deflections. This may be related again to the relatively small number of off-great circle 4.6 MHz signals when compared to the other frequencies.

Figure 9 shows the discrete distribution density of local winter signals versus Doppler spread (1 Hz bins) and deflection from the great circle heading (8° bins) for (a) 4.6, (b) 7.0, (c) 8.0, (d) 10.4, (e) 11.1, and (f) 14.4 MHz. Similar to Doppler shift, the peak distribution density occurs at zero Doppler spread and zero deflection from the GCH for all frequencies. Signals with higher Doppler spreads are observed at all frequencies primarily at non-zero deflection angles from the GCH. These high Doppler spread signals generally fall in two bands, one at positive deflection angles, and one at negative deflection angles. The width and horizontal location of these bands likely just indicate the deflection angles most off-great circle signals arrived at (also seen in Figure 4). The range of Doppler spreads with appreciable distribution density increases with frequency up to 11.1 MHz, with the range for 14.4 MHz somewhat lessened. Doppler spreads of up to ~ 24 Hz are observed at 4.6 MHz, while Doppler spreads of up to ~ 35 Hz are observed at 11.1 MHz. Similar to Figure 8, 4.6 MHz signals with negative deflections are seen to lead to larger Doppler spreads than signals with positive deflections.

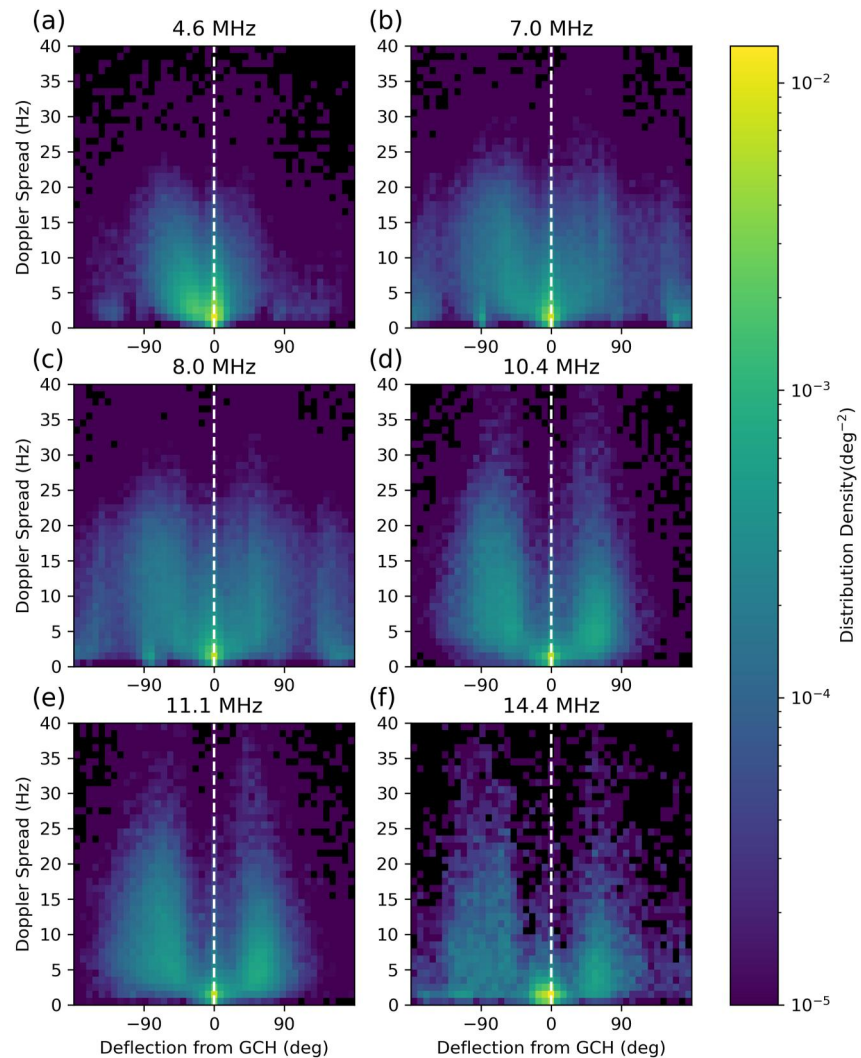


Figure 9. Discrete distribution density of received signals versus Doppler spread and deflection from the great circle heading for (a) 4.6, (b) 7.0, (c) 8.0, (d) 10.4, (e) 11.1, (f) 14.4 MHz. All distributions are plotted with a logarithmic color scale to better highlight off-great circle signals. Only radio signals received during local winter were counted. Zero deflection is indicated by a vertical white dashed line.

Figure 10 shows the discrete distribution density of local winter signals versus SNR (1.0 dB bins) and deflection from the GCH (8° bins) for (a) 4.6, (b) 7.0, (c) 8.0, (d) 10.4, (e) 11.1, and (f) 14.4 MHz. All frequencies show a peak in distribution density at close to zero deflection. This peak extends from 30 to 35 dB SNR for 4.6–8.0 MHz, while it is much more tightly focused around 35 dB for 10.4–14.4 MHz. For deflections away from zero, the distribution density at all frequencies is lower, and ranges in SNR from 0 to approximately 35 dB. The 4.6 MHz distribution is an exception to this pattern, where appreciable distribution density only reaches as low as approximately 10 dB for off-great circle signals. This is probably due to the comparative low number of off-great circle signals received at 4.6 MHz compared to the other frequencies (seen in Figure 4).

Focusing on SNR < 25 dB for the higher five frequencies, there is appreciable distribution density in three distinct bands extending downwards in SNR to –15 dB. These bands are separated by relative gaps in distribution density. One 10° wide band is centered around zero deflection, with more distribution density negative of zero. The other two bands span approximately –150° to –45°, and 30° to 100° in deflection from the GCH, though they widen slightly with decreasing SNR. The negative deflection band is generally wider than the positive deflection band at all frequencies.

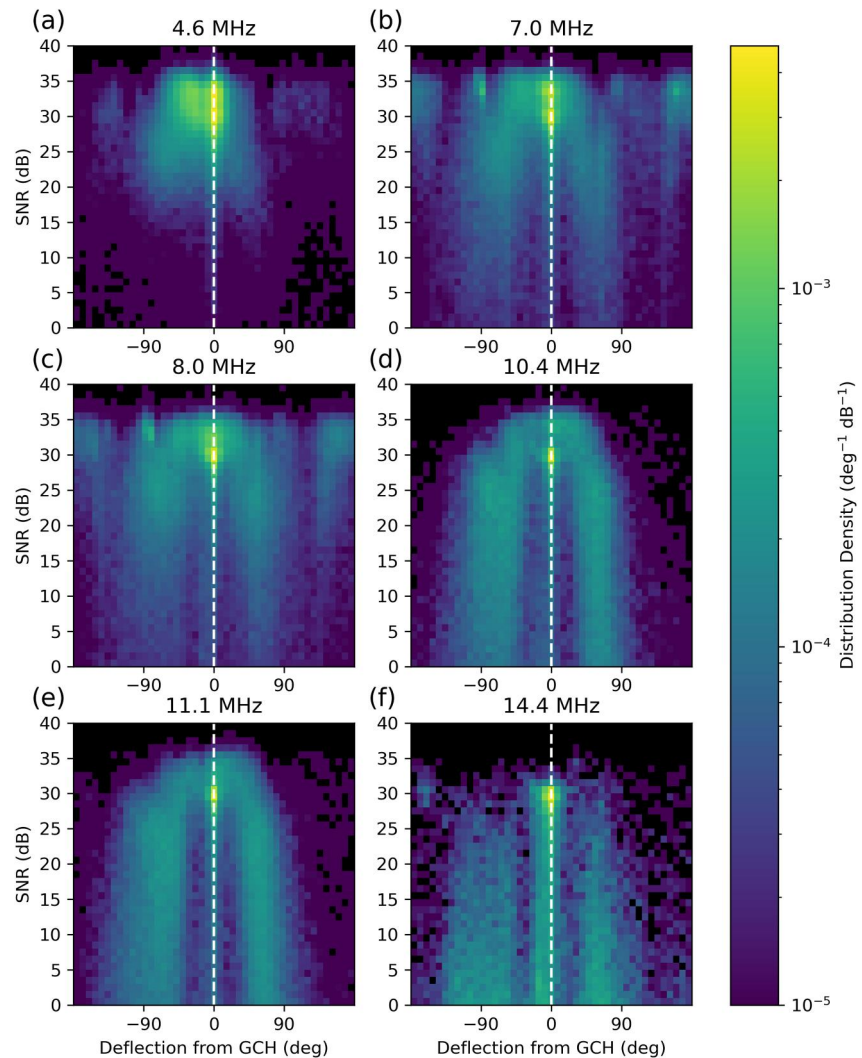


Figure 10. Discrete distribution density of received signals versus SNR and deflection from the great circle heading for (a) 4.6, (b) 7.0, (c) 8.0, (d) 10.4, (e) 11.1, (f) 14.4 MHz. All distributions are plotted with a logarithmic color scale to better highlight off-great circle signals. Only radio signals received during local winter were counted. Zero deflection is indicated by a vertical white dashed line.

Because there is comparable distribution density for on and off-great circle signals at low SNR, it is hard to tell from Figure 10 if off-great circle signals tend to have low SNR more often than on-great circle signals. It is possible that they do, but the generally higher occurrence of on-great circle signals leads to similar occurrence frequencies. To untangle this, the pointwise mutual information (PMI) between SNR and deflection from the GCH can be calculated (Lizier, 2014). PMI is defined as

$$\text{PMI}(x; y) = \log_2 \left(\frac{p(x, y)}{p(x)p(y)} \right), \quad (1)$$

where $p(x)$ and $p(y)$ refer to the probability distributions of the random variables X and Y respectively, and $p(x, y)$ is the joint probability distribution of X and Y . PMI quantifies whether specific values of x and y occur together more or less often than would be expected if their distributions were independent, such that a PMI of n bits means the corresponding x and y values occur together 2^n times as often. In this case, $p(x)$ and $p(y)$ are approximated with 1D histograms of deflection and SNR respectively, while $p(x, y)$ is approximated with the 2D histogram of both. Cameron et al. (2019) contains a more detailed explanation of PMI, as well as a few illustrative examples of its utility.

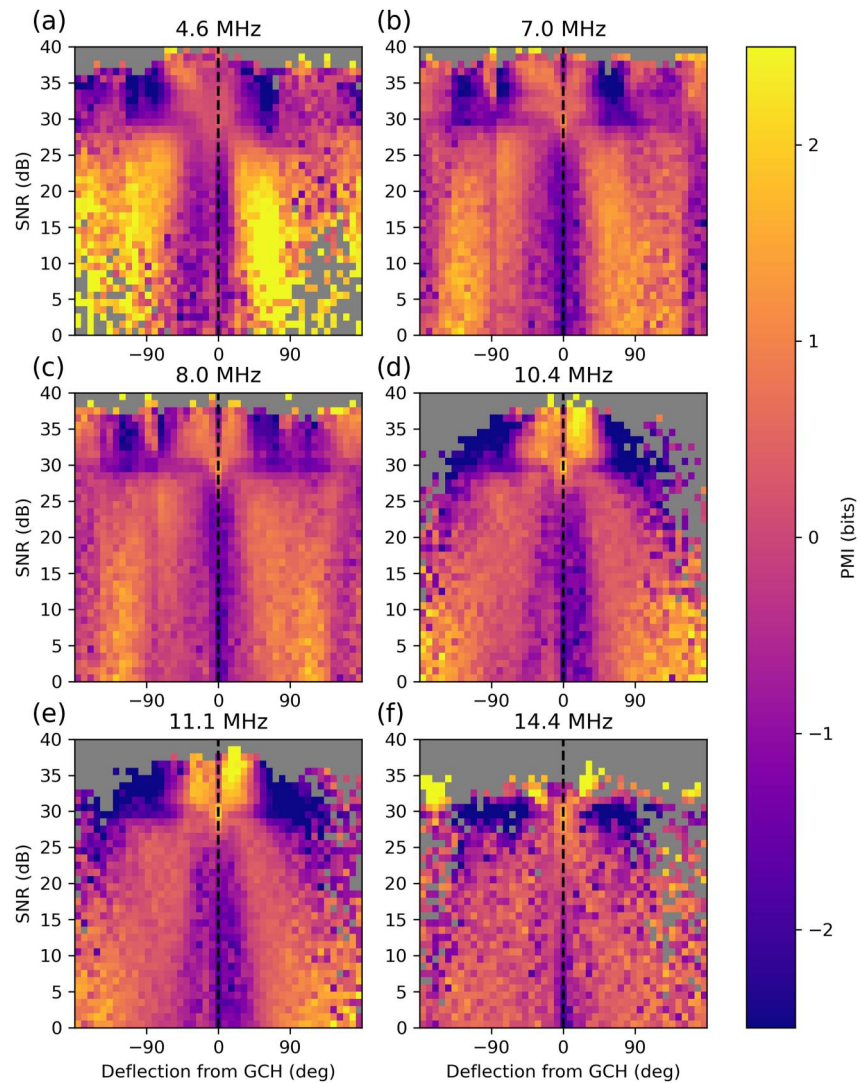


Figure 11. Pointwise mutual information between SNR and deflection from the great circle heading for (a) 4.6, (b) 7.0, (c) 8.0, (d) 10.4, (e) 11.1, (f) 14.4 MHz. Only radio signals received during local winter were counted. Zero deflection is indicated by a vertical black dashed line, and bins with no data are indicated with gray.

Figure 11 shows the PMI between SNR and deflection from the great circle heading for (a) 4.6, (b) 7.0, (c) 8.0, (d) 10.4, (e) 11.1, and (f) 14.4 MHz. The histograms used to calculate PMI used the same bin widths as Figure 10. At every frequency, the PMI shows that off-great circle signals are much more likely to have SNR < 30 dB, while on-great circle signals are much less likely to have SNR < 30 dB. The apparently high distribution density of low SNR, on-great circle signals is simply because so many more on-great circle signals were recorded than off-great circle signals. Interestingly, the PMI for SNR > 30 dB is highest for deflections between -45° and 45° , with a clear gap at 0° . This suggests that the signals with the highest SNR experienced non-zero deflections of less than 45° more often than expected.

5. Discussion

In this study, off-great circle propagation in the polar cap was studied using nearly 2.5 years of data from a polar cap HF radio link. An example of a day of patch affected HF propagation was presented in Section 3. Repeated ~ 30 to -60 min long swings in the azimuthal angle of arrival occurred in two periods during the day when IMF B_z was negative. These swings were attributed to polar cap patches crossing the propagation path. As each patch

approached, crossed, and then receded from the propagation path, the azimuthal angles of radio waves that reflected off the patch and reached the receiver changed smoothly from one side of the GCH to the other.

The orientation of the azimuthal swings reversed for patches observed 01:30–12:00 UT and 18:00–24:00 UT, which can be explained by the rotation of the Earth under the polar cap convection pattern, illustrated in the right panel of Figure 1. During the first period, patches moving with ionospheric convection from the dayside to nightside of the Earth crossed the QAN–ALE path from roughly east to west, resulting in azimuthal swings from below to above the GCH (see 08:00 UT in Figure 1). During the second period, which was ~12 hr later, the Earth and the QAN–ALE path had rotated under the convection pattern so that patches crossed from west to east, and the corresponding swings were in the opposite direction (22:00 UT in Figure 1).

The effects these deflections had on other parameters are also consistent with the patch crossings. Signals with larger deflections from the GCH traveled longer paths to reach Alert, leading to larger TOFs. Positive to negative Doppler shift swings are the result of reflection off the moving patches. As a patch approaches perpendicular to the path, the reflected radio waves experience Doppler shifts that get progressively smaller, since the component of the patches' velocity parallel to the wave propagation direction decreases with the magnitude of deflection. As the patch recedes, the reflected radio waves experience negative Doppler shifts that get progressively larger. This pattern is the same regardless of which side the patches approach from, explaining why the Doppler shifts are positive to negative during both periods. Increased Doppler spreads may be caused by the interaction of the HF radio waves with spatial structuring associated with patches.

There is an asymmetry in the azimuthal swings (relative to the GCH) and associated Doppler shifts during the beginning of the second negative IMF B_z period that was not seen during the first. This asymmetry may be because the Qanaaq to Alert path was at an oblique angle relative to the convection flow during this time, affecting both the azimuthal swings and the Doppler shifts. Patches or arcs moving near the propagation path but not directly crossing would lead to partial swings entirely on one side of the GCH, and entirely positive or entirely negative Doppler shifts.

During the period when IMF B_z was positive, less structured deflections were still observed at all frequencies. Accompanying Doppler shifts were generally low and negative during this period. This behavior is also consistent with ionospheric convection. When IMF B_z turns positive, ionospheric convection largely slows, but patches don't immediately disappear. These deflections and accompanying Doppler shifts could be caused by deflections off of decaying, still-moving patches. It is also possible that some deflections during this time are due to interactions with a polar cap arc, since polar cap arcs are associated with positive IMF B_z .

In Section 4.1, a mostly uninterrupted year of QAN–ALE transmission data was used to quantify the occurrence and magnitude of polar cap off-great circle propagation. The distribution of HF radio signal deflections across the year for 6 frequencies from 4.6 to 14.4 MHz (Figure 4) showed that deflections from the GCH are common, and that the occurrence and magnitude of these deflections increase with frequency up to at least 11.1 MHz. This behavior is consistent with the supposition that polar cap patches and arcs are responsible for these deflections. 4.6 MHz waves are reflected back toward the ground at a lower altitude than higher frequency waves, rarely reaching a high enough altitude to have their trajectories altered by patches or arcs. Higher frequency waves are able to penetrate higher into the ionosphere, and are more likely to interact with patches or arcs. If the wave frequency is too high however, these waves may pass through patches or arcs completely, escaping to space. This may explain the lower occurrence of off-great circle deflections for 14.4 MHz compared to 11.1 MHz. Since polar cap arcs have been known to occur at E-region altitudes, it is possible that lower frequencies are more likely to experience deflections caused by arcs than patches, since patches are primarily F-region phenomena.

Plots of the weekly median magnitude of deflection showed that deflections were largest in the local winter and were close to zero in the summer, for frequencies up to 11.1 MHz. Plots of the median magnitude of deflection signals binned by hour of the day (UT) and day of year showed that deflections for frequencies up to 8.0 MHz peaked in the UT morning (~06:00 UT) across local winter. Deflections for 11.1 MHz signals also peaked in the UT morning at the beginning and end of local winter. Near the winter solstice however, 11.1 MHz median deflections were found to be close to zero from 02:00–14:00 UT, and high (generally $>50^\circ$) for the rest of the day. The observation that deflections are highest in the winter months and close to zero in the summer months is consistent with polar cap patch occurrence statistics reported for the Northern Hemisphere by Noja et al. (2013),

Spicher et al. (2017), and Chartier et al. (2018), who all observed that patch occurrence is highest in the winter months and close to zero in the summer months.

Comparison of the observed distribution of off-great circle deflections across the day with patch occurrence statistics requires some care, since more factors than just the occurrence of ionospheric enhancements affect the occurrence of deflections. For a signal to experience a deflection from a patch, the wave frequency must be high enough compared to the background electron density to reach the F-region, but still low enough relative to the patch density that it experiences a deflection instead of escaping to space. Since 11.1 MHz signals experienced deflections more often than the other frequencies, the distribution of 11.1 MHz deflections across the day is most likely to match up with studies of patch occurrence. A study of the occurrence rate of patches using local winter (January–March and September–December) observations from the Resolute Bay Incoherent Scatter Radar-Canada (RISR-C) (Ren et al., 2018) reported that 60% of patches were observed from 1200 to 2400 MLT (19:00 to 07:00 UT), with the maximum patch occurrence occurring from 21:00 to 02:00 UT. This is approximately consistent with the observed distribution of 11.1 MHz deflections, since deflections were only observed consistently across the entire winter from 14:00 to 02:00 UT and only at the beginning and end of winter at other times.

David et al. (2016, 2019) investigated polar cap patch occurrence with respect to UT time and day of year with maps of TEC. In both studies, they found that in the Northern Hemisphere, patches were most common around 00:00–12:00 UT near the spring and fall equinoxes. In the middle of winter however, patch occurrence was close to zero from around 02:00–12:00 UT, and high after 12:00 and before 02:00 UT. Kagawa et al. (2021) observed a similar pattern studying patch occurrence with in-situ plasma density measurements, where patches were most common near the solstice from 15:00–24:00 UT. Results from all three studies match the occurrence of 11.1 MHz deflections well, and all report the same “hole” in patch occurrence near the solstice in the UT morning (e.g., Figure 3 from David et al. (2019)). These studies attribute variation in patch occurrence across the day and year to an explanation of patch formation in which patches are created when high density, sunlit plasma is drawn into the lower density polar cap by the polar cap convection pattern. According to this explanation, patch occurrence is highest during times when most of the polar cap is in darkness, but there is still significant overlap between the solar terminator and the polar cap convection pattern. The “hole” in the winter patch distribution exists because near the winter solstice, polar cap convection can only draw in lower density nightside plasma because the solar terminator is too far south. Figure 4 in David et al. (2019) shows this clearly with patch-to-background ratios calculated from Utah State University Time Dependent Ionospheric Model (TDIM) runs for different times of day and year, based on earlier work by Sojka et al. (1993). This “hole” is also present in climatological observations of TEC irregularities reported by Jin et al. (2022).

The correspondence of 11.1 MHz deflections to patch occurrence with respect to UT and time of year suggests that a significant amount of these deflections are caused by polar cap patches. The distribution of deflections at other frequencies can be compared to patch occurrence as well, given the other factors affecting the occurrence of deflections. The 14.4 MHz distribution of deflections also lines up approximately with the patch distribution whenever enough signals were received to calculate median deflections, except there is a drop in deflections in the UT evening near solstice compared to 11.1 MHz. This could be because the patch-to-background ratio at this time is expected to be lower than the surrounding weeks (seen in Figure 4 of David et al. (2019)), meaning 14.4 MHz waves are deflected less, but 11.1 MHz waves are not at a high enough frequency to be affected.

The deflection distributions for the lower three frequencies do not show a “hole” in the winter solstice UT morning at all. This difference between the lower and higher frequency UT distributions suggests that the lower frequency deflections at this time are caused by ionospheric electron density enhancements with peak densities too low to deflect 11.1 MHz signals, but still high enough relative to the background density to deflect 8.0 MHz and lower signals. These enhancements could be too low density to be considered patches according to the classical definition (twice the background density), explaining their absence from patch occurrence trends. They could, for example, be the result of plasma ionized by electron precipitation in the auroral region, or simply higher density plasma closer to the solar terminator, being drawn into the polar cap by convection. Some of these low frequency deflections could be due to polar cap arcs as well.

The final part of this study investigated the effect off-great circle deflections have on other signal characteristics. Signals that experienced large positive and negative deflections from the GCH tended to have larger TOFs, a larger range of possible positive and negative Doppler shifts, and larger Doppler spreads. The connection between

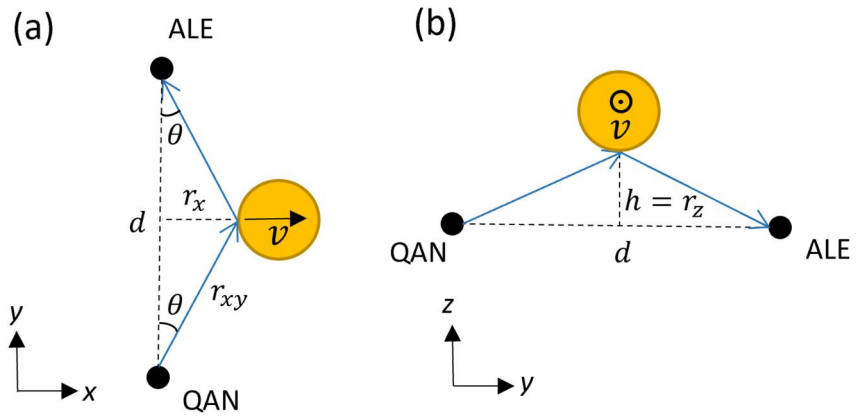


Figure 12. Diagram showing an idealized 1-hop vertical reflection with lateral deflection off of an electron density enhancement. The left side (a) shows a top-down view, while the right side (b) shows a vertical view.

SNR and deflection from the GCH was hard to untangle from the occurrence of deflections, but an analysis of the PMI between the two showed that signals with larger deflections were more likely to have lower SNRs than what would be expected if the two quantities were independent.

A simple, illustrative model of localized density enhancements crossing the QAN–ALE propagation path can be used to explain the shapes of the TOF - deflection distributions seen in Figure 7. These enhancements could be polar cap patches, polar cap arcs, or any other localized electron density structure capable of reflecting HF radio waves. In this model, the QAN–ALE propagation path is aligned along the y axis, and the z direction is corresponds to straight up. A localized electron density enhancement at a height h crosses the QAN–ALE propagation path exactly halfway between the two locations, moving at some velocity v in the x direction. Meanwhile, an HF radio signal leaves the QAN transmitter at the azimuthal and elevation angles required to reach the enhancement, reflects off it, and then reaches the ALE receiver. In order to simplify the model, it is assumed that the refractive index is 1 (meaning the signal travels in a straight line at the speed of light) before and after reflection. In reality, the speed of an HF radio wave varies as it travels through the ionosphere. However, this effect only becomes significant near the reflection point for the signal. This model can be thought of as a limiting case for the actual dependence of TOF on deflection angle. The simplifying assumptions made about the enhancement crossing exactly halfway between QAN and ALE, moving exactly perpendicular to the path, are likely larger sources of error than assuming signals travel at the speed of light. Figure 12 illustrates the coordinate system, and the geometry of the one-hop propagation, with the horizontal deflection off the patch on the left (a), and the vertical reflection on the right (b).

The expected TOF for the radio signal is simply twice the length of the vector from QAN to the enhancement ($r = \sqrt{r_{xy}^2 + r_z^2}$) divided by the speed of light (c). Referring to Figure 12, the horizontal component of this vector (r_{xy}) is $\frac{d/2}{\cos(\theta)}$, where d is the distance from QAN to ALE, and θ is the deflection from the GCH. The vertical component of the vector from QAN to the enhancement (r_z) is simply the reflection height h . Therefore,

$$r = \sqrt{h^2 + \frac{d^2}{4\cos^2\theta}} \quad (2)$$

and the expected TOF is

$$\text{TOF}(\theta) = \frac{2}{c} \sqrt{h^2 + \left(\frac{d/2}{\cos\theta}\right)^2} \quad (3)$$

Overlaid in red and light blue on each panel in Figure 7 is the expected TOF as a function of deflection angle, assuming the one-hop deflection described in Equation 3. The red curves were calculated assuming a reflection

height of 300 km (F-region) for deflections between -90° and 90° , while the blue curves were calculated assuming a reflection height of 100 km (E-region) for deflections between -45° and 45° . In each panel, the red TOF curves overlay the densest parts of the higher TOF population, suggesting that this part of the distribution is due to reflection off of F-region electron density enhancements such as polar cap patches or arcs. The spread around the red curves is likely due to variability in the reflection height over time. The light blue curves overlap the lower TOF population for deflections between -30° to 30° deflection, but predicts a higher TOF than the lower population indicates for deflections larger than that. These E-region azimuthal deflections could be due to low altitude arcs, but the separation between the two populations suggests an exclusively E-region phenomenon. Sporadic-E layers have been known to exhibit tilts of up to $\sim 20^\circ$ or more with respect to the horizon (e.g., From & Whitehead, 1978; Parkinson & Dyson, 1998; Paul, 1990). It is possible that some deflections in the lower TOF population are due to reflections off of tilted sporadic-E layers. There are also $>90^\circ$ deflection signals in Figure 7, especially for the lower three frequencies, with lower TOFs than would be expected. These signals are possibly on-great circle signals that were deflected by nearby electron density enhancements drifting behind the receiver. They could also be signals that experienced local deflections near the receiver before being recorded.

This simple model can also be used to explain the shape of the Doppler shift - deflection distributions seen in Figure 8. The total Doppler shift experienced by an HF radio wave in the ionosphere is the accumulation of Doppler shifts experienced along the path as the wave travels through a non-stationary medium. In Figure 8, on-great circle signals for all frequencies experience little to no Doppler shift, suggesting that the majority of Doppler shifts are connected to azimuthal deflections. This is consistent with the simplifying assumption that the signal is in vacuum before and after reflection, and the total Doppler shift is entirely due to reflection off the density enhancement. The expected Doppler shift of a signal reflected off a surface moving parallel to the signal is

$$\Delta f = \frac{2v_r f}{c}, \quad (4)$$

where v_r is the component of the velocity of the surface parallel to the wave vector, and f is the frequency of the wave. Since the electron density enhancement is moving in the x direction, the component of the enhancement velocity parallel to wave vector can be expressed as

$$v_r = v \frac{r_x}{r}, \quad (5)$$

where v is the speed of the enhancement, r is the length of the vector from QAN to the enhancement, and r_x is the x component of that vector. r was found above in Equation 2, and $r_x = \frac{d}{2} \tan(\theta)$ based on Figure 12. Pulling these together,

$$v_r(\theta) = v \frac{d \tan \theta}{2\sqrt{h^2 + \frac{d^2}{4\cos^2\theta}}}, \quad (6)$$

and the expected Doppler shift is

$$\Delta f(\theta) = \frac{vf}{c} \frac{d \tan \theta}{\sqrt{h^2 + \frac{d^2}{4\cos^2\theta}}}, \quad (7)$$

Overlaid on Figure 8 in red are curves showing Doppler shift versus deflection assuming a reflection height of 300 km, for enhancements moving at ± 600 m/s relative to Qaanaaq and Alert. This speed is near the upper limit of possible speeds for an ionospheric density enhancement relative to the propagation path. It is the sum of the upper end of the distribution of polar cap patch speeds measured by Hosokawa et al. (2009) (~ 500 m/s), and the rotation speed of the Earth at the latitude of Qaanaaq (~ 100 m/s). In reality, these enhancements could be moving at a variety of speeds lower than 500 m/s, and at oblique angles relative to the propagation path, which in both cases

would result in smaller Doppler shifts. Therefore, the red curves in Figure 8 can be considered upper limits on possible Doppler shifts for this radio link.

The Doppler shift curves bound the distributions of Doppler shifts at all frequencies well. An analysis of the data set showed that these Doppler shift limits bound at least 89% of signals with positive and negative deflections from the GCH between 2° and 90° for all frequencies, and at least 97% for the upper three frequencies. For the three lower frequencies, the distribution density does not reach the Doppler shift curves for deflection angles close to 90°. This is probably because there were not enough signals received at these deflection angles for an appreciable amount to have reflected off density enhancements moving perpendicular to the QAN–ALE line at sufficient speeds.

One final consideration that could influence the effect of off-great circle deflections on HF radio signal parameters is vertical motion of electron density enhancements. The drift of polar cap patches via ionospheric convection occurs due to an $\mathbf{E} \times \mathbf{B}$ drift involving the convection electric field and the Earth's magnetic field. There is a non-zero vertical component to this drift wherever magnetic field lines are not oriented vertically, meaning patches tend to move upwards when drifting toward the pole and downwards after crossing the pole with speeds of tens of m/s (Hosokawa et al., 2019; Perry et al., 2013). If the reflection height changes with a constant speed,

$$h(\theta) = h_0 + v_v \frac{d}{2v} \tan(\theta) \quad (8)$$

where h_0 is the reflection height at the crossing point, and v_v is the vertical drift speed. Inserting this into Equation 3 shows that a vertical drift speed of even 100 m/s (with an h_0 of 300 km) does not result in a perceptible difference in the expected TOF. An additional vertical drift changes the expected Doppler shift equation, since it changes the component of the enhancement velocity relative to the wave vector. Accounting for vertical motion, this component is

$$v_r = v \frac{r_x}{r} + v_v \frac{r_z}{r} = \frac{vr_x + v_v h(\theta)}{r}, \quad (9)$$

and the expected Doppler shift becomes

$$\Delta f(\theta) = \frac{f}{c} \frac{vd \tan \theta + 2v_v h(\theta)}{\sqrt{h(\theta)^2 + \frac{d^2}{4\cos^2 \theta}}}. \quad (10)$$

As with TOF, a vertical drift speed of even 100 m/s with $h_0 = 300$ km leads to an imperceptible difference in Doppler shift, at least for the simple patch crossing model described here.

6. Conclusions

This study evaluated nearly 2.5 years of 4.6–14.4 MHz radio propagation data from a high-latitude HF radio link to study off-great circle propagation in the polar cap region. A single day of received HF radio signals in which polar cap patch activity occurred was presented to establish how polar cap density enhancements can cause deflections from the expected angle of arrival. “Swings” in the azimuthal angle of arrival relative to the great circle heading (GCH); previously connected to polar cap patch crossings (Warrington et al., 1997), occurred during the parts of the day when the IMF B_z was negative. These swings were shown to be concurrent with time-of-flight (TOF) increases, Doppler shifts that transitioned from up to 30 Hz to as low as –25 Hz, and enhanced Doppler spreads of up to 65 Hz.

To determine the prevalence and magnitude of these deflections in general, a statistical analysis was performed. Examination of the distribution of signal deflections from the GCH for a largely uninterrupted year of transmissions showed that off-great circle propagation is commonly observed in the high-latitude ionosphere, and becomes increasingly prevalent with increasing frequency up to 11.1 MHz. This is because higher frequencies reach the F-region ionosphere more often, and can therefore be deflected by F-region density structures more often than lower frequencies. From April 2013 to April 2014, received 11.1 MHz signals arrived with deflections

from the GCH of $>30^\circ$ 65.6% of the time. The prevalence of these large deflections are highly dependent on time of day and year. An analysis of the weekly median magnitude of deflections over the year indicated that median deflections are largest in the winter for all frequencies, and tend to be close to zero in the summer. Further investigation of the prevalence of deflections versus UT time of day at different times of year showed that deflections for lower frequencies (4.6–8.0 MHz) are most common in the morning across the winter, while high frequencies (11.1–14.4 MHz) experience little to no deflections in the morning near the winter solstice. The high frequencies do experience significant deflections in the morning at the beginning and end of winter, however. The variation of deflections with respect to time of day and time of year for the high frequencies are consistent with a theory of patch generation involving dayside plasma being drawn into the polar cap by convection. The difference in UT distributions between high and low frequencies suggests a significant amount of lower frequency deflections (at least near the winter solstice) are due to electron density enhancements with peak densities or peak-to-background ratios too low to be considered polar cap patches.

An analysis of the full 2.5-year data set showed how the following HF radio signal properties change when the signals undergo large deflections from the GCH:

- Signals deflected to off-great circle paths have generally larger TOFs, due to their necessarily longer propagation paths. The rate of increase in TOF with deflection is consistent with a simple model of reflection off of drifting localized enhancements at F-region altitudes crossing between QAN and ALE.
- The range of observed Doppler shifts is strongly dependent on deflection from the GCH, where larger deflections have a larger range of possible positive and negative Doppler shifts. This dependence is consistent with the same simple model of reflection off of drifting F-region enhancements, assuming the enhancements have drift speeds of up to 600 km/s relative to the propagation path.
- Off-great circle signals are associated with increased Doppler spreads, with spreads of up to ~ 35 Hz observed for 11.1 MHz signals.
- An analysis of the pointwise mutual information (PMI) between deflection from the GCH and signal-to-noise ratio (SNR) showed that signals with deflections of $>\sim 20$ deg are more likely to have SNRs of $<\sim 30$ dB. Conversely, signals with deflections of $<\sim 20$ deg are more likely to have SNRs of $>\sim 30$ dB.

Over-the-horizon radar (OTHR) operation is particularly sensitive to the deflection of HF radio waves to off-great circle paths and the accompanying TOF changes, since locating a target with OTHR requires knowledge of the propagation path to the target. These results suggest that any OTHR performing surveillance in the polar cap will frequently have to account for off-great circle deflections, especially in the winter. Left unaddressed, these deflections could lead to increased uncertainty in target location, while associated Doppler shifts and spreads could introduce uncertainty to velocity determination as well. As mentioned in the introduction, research is ongoing on how polar cap density enhancements affect OTHR coverage (Thayaparan et al., 2020, 2021). The results shown here could inform future research focused on mitigating the effects of off-great circle propagation on OTHR.

These results also represent a likely significant challenge for scientific OTHRs that are subject to polar HF radio propagation conditions—such as the polar component of the Super Dual Auroral Radar Network (SuperDARN). Off great-circle path deviations with SuperDARN radars have been reported in the past (e.g., Perry et al., 2016), but have not yet been specified or characterized with that system. Adding to the challenges is the fact that a reliable technique for identifying patches or instances of great-circle propagation has not yet been developed for the SuperDARN system. SuperDARN geolocation algorithms assume great-circle propagation (Chisham et al., 2008) which—as our results show—is often not the case in the polar-cap region. Studies are currently underway to determine the degree to which SuperDARN geolocation can be affected by off great-circle path deviations.

Data Availability Statement

QAN–ALE HF radio data for 2012–2016 are available online at the Harvard Dataverse (<https://doi.org/10.7910/DVN/RGDNR1>). OMNI data can be accessed via NASA's Coordinated Data Analysis Web (<https://cdaweb.gsfc.nasa.gov/>). CHAIN ionosonde data can be found on the CHAIN website (http://chain.physics.unb.ca/chain/pages/data_download).

Acknowledgments

This project was supported by TPA 03–2022 between the DRDC and NRCan under MoU 2018070005 between the DND and NRCan. GWP is supported by the NASA Living with a Star Grant 80NSSC21K1318. AS acknowledges the Research Council of Norway (RCN) Grant 326039 and the UiT The Arctic University of Norway contribution to the EISCAT3D project (RCN funded research infrastructure Grant 245683). The authors would like to thank Dr. David Themens for processing the CHAIN ionosonde data presented in Figure 2. The authors would also like to thank Dr. Donald Danskin for helpful discussions and advice. Infrastructure funding for CHAIN was provided by the Canada Foundation for Innovation and the New Brunswick Innovation Foundation. CHAIN and its operation are conducted in collaboration with the Canadian Space Agency. We acknowledge use of NASA/GSFC's Space Physics Data Facility's ftp service, and OMNI data. This is NRCan publication number 20220558. Open Access funding provided by the Natural Resources Canada library.

References

- Berkey, F. T., Cogger, L. L., Ismail, S., & Kamide, Y. (1976). Evidence for a correlation between Sun-aligned arcs and the interplanetary magnetic field direction. *Geophysical Research Letters*, 3(3), 145–147. <https://doi.org/10.1029/GL003i003p00145>
- Burtnyk, N., McLeish, C. W., & Wolfe, J. (1962). Ionosphere layer tilts at Ottawa, Canada. *Canadian Journal of Physics*, 40(11), 1614–1619. <https://doi.org/10.1139/p62-167>
- Cameron, T. G., Fiori, R. A., Warrington, E. M., Stocker, A. J., Thayapan, T., & Danskin, D. W. (2021). Characterization of high latitude radio wave propagation over Canada. *Journal of Atmospheric and Solar-Terrestrial Physics*, 219, 105666. <https://doi.org/10.1016/j.jastp.2021.105666>
- Cameron, T. G., Jackel, B., & Oliveira, D. M. (2019). Using mutual information to determine geoeffectiveness of solar wind phase fronts with different front orientations. *Journal of Geophysical Research: Space Physics*, 124(3), 1582–1592. <https://doi.org/10.1029/2018JA026080>
- Chartier, A. T., Mitchell, C. N., & Miller, E. S. (2018). Annual occurrence rates of ionospheric polar cap patches observed using Swarm. *Journal of Geophysical Research: Space Physics*, 123(3), 2327–2335. <https://doi.org/10.1002/2017JA024811>
- Chisham, G., Yeoman, T. K., & Sofko, G. J. (2008). Mapping ionospheric backscatter measured by the SuperDARN HF radar—Part 1: A new empirical virtual height model. *Annales Geophysicae*, 26(4), 823–841. <https://doi.org/10.5194/angeo-26-823-2008>
- Coley, W. R., & Heelis, R. A. (1995). Adaptive identification and characterization of polar ionization patches. *Journal of Geophysical Research*, 100(A12), 23819–23827. <https://doi.org/10.1029/95ja02700>
- Coley, W. R., & Heelis, R. A. (1998). Seasonal and universal time distribution of patches in the northern and southern polar caps. *Journal of Geophysical Research*, 103(A12), 29229–29237. <https://doi.org/10.1029/1998JA900005>
- Crowley, G. (1996). Critical review of ionospheric patches and blobs. In W. Stone (Ed.), *Review of radio science 1992–1996* (pp. 619–648). Oxford University Press.
- Dahlgren, H., Perry, G. W., Semeter, J. L., St-Maurice, J.-P., Hosokawa, K., Nicolls, M. J., et al. (2012). Space-time variability of polar cap patches: Direct evidence for internal plasma structuring. *Journal of Geophysical Research*, 117(A9), A09312. <https://doi.org/10.1029/2012JA017961>
- David, M., Sojka, J., Schunk, R., & Coster, A. (2019). Hemispherical shifted symmetry in polar cap patch occurrence: A survey of GPS TEC maps from 2015–2018. *Geophysical Research Letters*, 46(19), 10726–10734. <https://doi.org/10.1029/2019GL083952>
- David, M., Sojka, J. J., Schunk, R. W., & Coster, A. J. (2016). Polar cap patches and the tongue of ionization: A survey of GPS TEC maps from 2009 to 2015. *Geophysical Research Letters*, 43(6), 2422–2428. <https://doi.org/10.1002/2016GL068136>
- Fear, R. C., & Milan, S. E. (2012). The IMF dependence of the local time of transpolar arcs: Implications for formation mechanism. *Journal of Geophysical Research*, 117(A3), A03213. <https://doi.org/10.1029/2011JA017209>
- From, W. R., & Whitehead, J. D. (1978). On the peculiar shape of sporadic-E clouds. *Journal of Atmospheric and Terrestrial Physics*, 40(9), 1025–1028. [https://doi.org/10.1016/0021-9169\(78\)90006-5](https://doi.org/10.1016/0021-9169(78)90006-5)
- Goodwin, L. V., Isernhien, B., Miles, D. M., Patra, S., van der Meeren, C., Buchert, S. C., et al. (2015). Swarm in situ observations of F region polar cap patches created by cusp precipitation. *Geophysical Research Letters*, 42(4), 996–1003. <https://doi.org/10.1002/2014GL062610>
- Hosokawa, K., Kashimoto, T., Suzuki, S., Shiokawa, K., Otsuka, Y., & Ogawa, T. (2009). Motion of polar cap patches: A statistical study with all-sky airglow imager at Resolute Bay, Canada. *Journal of Geophysical Research*, 114(4), 1–8. <https://doi.org/10.1029/2008JA014020>
- Hosokawa, K., Kullen, A., Milan, S., Reidy, J., Zou, Y., Frey, H. U., et al. (2020). Aurora in the polar cap: A review. *Space Science Reviews*, 216(1), 15. <https://doi.org/10.1007/s11214-020-0637-3>
- Hosokawa, K., Moen, J. I., Shiokawa, K., & Otsuka, Y. (2011). Motion of polar cap arcs. *Journal of Geophysical Research*, 116(A1), A01305. <https://doi.org/10.1029/2010JA015906>
- Hosokawa, K., Zou, Y., & Nishimura, Y. (2019). Airglow patches in the polar cap region: A review. *Space Science Reviews*, 215(8), 53. <https://doi.org/10.1007/s11214-019-0616-8>
- Jayachandran, P. T., Hosokawa, K., MacDougall, J. W., Mushini, S., Langley, R. B., & Shiokawa, K. (2009). GPS total electron content variations associated with a polar cap arc. *Journal of Geophysical Research*, 114(A12), A12304. <https://doi.org/10.1029/2009JA014916>
- Jayachandran, P. T., Hosokawa, K., Shiokawa, K., Otsuka, Y., Watson, C., Mushini, S. C., et al. (2012). GPS total electron content variations associated with poleward moving Sun-aligned arcs. *Journal of Geophysical Research*, 117(A5), A05310. <https://doi.org/10.1029/2011JA017423>
- Jayachandran, P. T., Langley, R. B., MacDougall, J. W., Mushini, S. C., Pokhotelov, D., Hamza, A. M., et al. (2009). Canadian High Arctic Ionospheric Network (CHAIN). *Radio Science*, 44(3), 1–10. <https://doi.org/10.1029/2008RS004046>
- Jin, Y., Clausen, L. B. N., Miloch, W. J., Høeg, P., Jarmołowski, W., Wielgosz, P., et al. (2022). Climatology and modeling of ionospheric irregularities over Greenland based on empirical orthogonal function method. *Journal of Space Weather and Space Climate*, 12, 23. <https://doi.org/10.1051/swsc/2022022>
- Jin, Y., Xing, Z., Zhang, Q., Wang, Y., & Ma, Y. (2019). Polar cap patches observed by the EISCAT svalbard radar: A statistical study of its dependence on the solar wind and IMF conditions. *Journal of Atmospheric and Solar-Terrestrial Physics*, 192, 104768. <https://doi.org/10.1016/j.jastp.2018.01.011>
- Kagawa, A., Hosokawa, K., Ogawa, Y., Ebihara, Y., & Kadokura, A. (2021). Occurrence distribution of polar cap patches: Dependences on UT, season and hemisphere. *Journal of Geophysical Research: Space Physics*, 126(1), e2020JA028538. <https://doi.org/10.1029/2020JA028538>
- King, J. H., & Papitashvili, N. E. (2005). Solar wind spatial scales in and comparisons of hourly Wind and ACE plasma and magnetic field data. *Journal of Geophysical Research*, 110(A2), A02104. <https://doi.org/10.1029/2004JA010649>
- King, J. H., & Papitashvili, N. E. (2020). OMNI 5-min data set. *NASA Space Physics Data Facility*. <https://doi.org/10.48322/GBPG-5R77>
- Kivanc, Ö., & Heelis, R. A. (1997). Structures in ionospheric number density and velocity associated with polar cap ionization patches. *Journal of Geophysical Research*, 102(A1), 307–318. <https://doi.org/10.1029/96JA03141>
- Lizier, J. T. (2014). Measuring the dynamics of information processing on a local scale in time and space. In M. Wibral, R. Vicente, & J. T. Lizier (Eds.), *Directed information measures in neuroscience* (pp. 161–193). Springer Berlin Heidelberg. https://doi.org/10.1007/978-3-642-54474-3_7
- Meek, J. H. (1949). Sporadic ionization at high latitudes. *Journal of Geophysical Research*, 54(4), 339–345. <https://doi.org/10.1029/JZ054i004p00339>
- Morgan, A. D. (1974). A qualitative examination of the effect of systematic tilts, in the ionosphere, on HF bearing measurements. *Journal of Atmospheric and Terrestrial Physics*, 36(10), 1675–1681. [https://doi.org/10.1016/0021-9169\(74\)90204-9](https://doi.org/10.1016/0021-9169(74)90204-9)
- Noja, M., Stolle, C., Park, J., & Lühr, H. (2013). Long-term analysis of ionospheric polar patches based on CHAMP TEC data. *Radio Science*, 48(3), 289–301. <https://doi.org/10.1002/rds.20033>

- Oksavik, K., Ruohoniemi, J. M., Greenwald, R. A., Baker, J. B., Moen, J., Carlson, H. C., et al. (2006). Observations of isolated polar cap patches by the European Incoherent Scatter (EISCAT) Svalbard and Super Dual Auroral Radar Network (SuperDARN) Finland radars. *Journal of Geophysical Research*, *111*(5), 1–9. <https://doi.org/10.1029/2005JA011400>
- Parkinson, M. L., & Dyson, P. L. (1998). Measurements of mid-latitude E-region, sporadic-E, and TID-related drifts using HF Doppler-sorted interferometry. *Journal of Atmospheric and Solar-Terrestrial Physics*, *60*(5), 509–522. [https://doi.org/10.1016/S1364-6826\(97\)00058-8](https://doi.org/10.1016/S1364-6826(97)00058-8)
- Paul, A. K. (1990). On the variability of sporadic E. *Radio Science*, *25*(1), 49–60. <https://doi.org/10.1029/RS025i001p00049>
- Perry, G. W., Miller, E. S., James, H. G., Howarth, A. D., St-Maurice, J. P., & Yau, A. W. (2016). HF radar transmissions that deviate from great-circle paths: New insight from e-POP RRI. In *AGU fall meeting abstracts* (p. SA44A-06).
- Perry, G. W., & St-Maurice, J.-P. (2018). A polar-cap patch detection algorithm for the advanced modular incoherent scatter radar system. *Radio Science*, *53*(10), 1225–1244. <https://doi.org/10.1029/2018RS006600>
- Perry, G. W., St-Maurice, J.-P., & Hosokawa, K. (2013). The interconnection between cross-polar cap convection and the luminosity of polar cap patches. *Journal of Geophysical Research: Space Physics*, *118*(11), 7306–7315. <https://doi.org/10.1002/2013JA019196>
- Ren, J., Zou, S., Gillies, R. G., Donovan, E., & Varney, R. H. (2018). Statistical characteristics of polar cap patches observed by RISR-C. *Journal of Geophysical Research: Space Physics*, *123*(8), 6981–6995. <https://doi.org/10.1029/2018JA025621>
- Riddolls, R. J. (2006). *A Canadian perspective on high-frequency over-the-horizon radar*. Defence R&D Canada.
- Ross, W., & Bramley, E. N. (1947). Lateral deviation of radio waves at sunrise. *Nature*, *159*(4030), 132. <https://doi.org/10.1038/159132a0>
- Sojka, J. J., Bowline, M. D., Schunk, R. W., Decker, D. T., Valladares, C. E., Sheehan, R., et al. (1993). Modeling polar cap F-region patches using time varying convection. *Geophysical Research Letters*, *20*(17), 1783–1786. <https://doi.org/10.1029/93GL01347>
- Spicher, A., Cameron, T., Grono, E. M., Yakymenko, K. N., Buchert, S. C., Clausen, L. B., et al. (2015). Observation of polar cap patches and calculation of gradient drift instability growth times: A swarm case study. *Geophysical Research Letters*, *42*(2), 201–206. <https://doi.org/10.1002/2014GL062590>
- Spicher, A., Clausen, L. B., Miloch, W. J., Lofstad, V., Jin, Y., & Moen, J. I. (2017). Interhemispheric study of polar cap patch occurrence based on Swarm in situ data. *Journal of Geophysical Research: Space Physics*, *122*(3), 3837–3851. <https://doi.org/10.1002/2016JA023750>
- Stocker, A. J., Warrington, E. M., & Siddle, D. R. (2013). Observations of Doppler and delay spreads on HF signals received over polar cap and trough paths at various stages of the solar cycle. *Radio Science*, *48*(5), 638–645. <https://doi.org/10.1002/2013RS005264>
- Tedd, B. L., Strangeways, H. J., & Jones, T. B. (1985). Systematic ionospheric electron density tilts (SITs) at mid-latitudes and their associated HF bearing errors. *Journal of Atmospheric and Terrestrial Physics*, *47*(11), 1085–1097. [https://doi.org/10.1016/0021-9169\(85\)90027-3](https://doi.org/10.1016/0021-9169(85)90027-3)
- Thayaparan, T., Ibrahim, Y., Polak, J., & Riddolls, R. (2018). High-frequency over-the-horizon radar in cCanada. *IEEE Geoscience and Remote Sensing Letters*, *15*(11), 1700–1704. <https://doi.org/10.1109/LGRS.2018.2856185>
- Thayaparan, T., Warrington, E. M., Stocker, A. J., & Siddle, D. R. (2021). Simulation of the effect of convecting patches of enhanced electron density on HF over-the-horizon radars (OTHRs) in the polar regions. *IEEE Geoscience and Remote Sensing Letters*, *18*(9), 1–5. <https://doi.org/10.1109/LGRS.2020.3045926>
- Thayaparan, T., Warrington, M., Stocker, A., & Siddle, D. (2020). Effect of frequency monitoring system for over-the-horizon radar due to the presence of patches and arcs within the polar cap ionosphere. In *Proceedings international radar symposium* (pp. 368–372). <https://doi.org/10.23919/IRS48640.2020.9253862>
- Valladares, C. E., Carlson, H. C., & Fukui, K. (1994). Interplanetary magnetic field dependency of stable sun-aligned polar cap arcs. *Journal of Geophysical Research*, *99*(A4), 6247–6272. <https://doi.org/10.1029/93JA03255>
- Warrington, E. M. (1998). Observations of the directional characteristics of ionospherically propagated HF radio channel sounding signals over two high latitude paths. *IEE Proceedings - Microwaves, Antennas and Propagation*, *145*(5), 379. <https://doi.org/10.1049/ip-map:19982068>
- Warrington, E. M., Rogers, N. C., & Jones, T. B. (1997). Large HF bearing errors for propagation paths contained within the polar cap. *IEE Proceedings - Microwaves, Antennas and Propagation*, *144*(4), 241–249. <https://doi.org/10.1049/ip-map:19971187>
- Warrington, E. M., Zaalov, N. Y., Naylor, J. S., & Stocker, A. J. (2012). HF propagation modeling within the polar ionosphere. *Radio Science*, *47*(3), 1–7. <https://doi.org/10.1029/2011RS004909>
- Weber, E. J., & Buchau, J. (1981). Polar cap F-layer auroras. *Geophysical Research Letters*, *8*(1), 125–128. <https://doi.org/10.1029/GL008i001p00125>
- Weber, E. J., Buchau, J., Moore, J. G., Sharber, J. R., Livingston, R. C., Winningham, J. D., & Reinisch, B. W. (1984). F layer ionization patches in the polar cap. *Journal of Geophysical Research*, *89*(A3), 1683–1694. <https://doi.org/10.1029/JA089iA03p01683>
- Zaalov, N. Y., Warrington, E. M., & Stocker, A. J. (2003). Simulation of off-great circle HF propagation effects due to the presence of patches and arcs of enhanced electron density within the polar cap ionosphere. *Radio Science*, *38*(3), 1–8. <https://doi.org/10.1029/2002RS002798>
- Zaalov, N. Y., Warrington, E. M., & Stocker, A. J. (2005). A ray-tracing model to account for off-great circle HF propagation over northerly paths. *Radio Science*, *40*(4), 1–14. <https://doi.org/10.1029/2004RS003183>